Stars and Planets

at

high spacial and spectral resolution

Stars and Planets

at

high spacial and spectral resolution

Proefschrift

ter verkrijging van
de graad van Doctor aan de Universiteit Leiden,
op gezag van de Rector Magnificus prof. mr. P.F. van der Heijden,
volgens besluit van het College voor Promoties
te verdedigen op Woensdag 17 december 2008
klokke 15.00 uur

door

Simon Albrecht

geboren te Osnabrück
in 1976

Promotiecommissie

Promotores: Prof. dr. A. Quirrenbach
Co-promotor: Dr. I.A.G. Snellen

Referent: Dr. M. Fridlund   (European Space Agency, ESTEC, Noordwijk)

Overige leden:

Contents

Chapter 1

Introduction

Chapter 2

A new concept for the combination of optical interferometers and high-resolution spectrographs

The combination of high spatial and spectral resolution in optical astronomy enables new observational approaches to many open problems in stellar and circumstellar astrophysics. However, constructing a high-resolution spectrograph for an interferometer is a costly and time-intensive undertaking. Our aim is to show that, by coupling existing high-resolution spectrographs to existing interferometers, one could observe in the domain of high spectral and spatial resolution, and avoid the construction of a new complex and expensive instrument. We investigate in this chapter the different challenges which arise from combining an interferometer with a high-resolution spectrograph. The requirements for the different sub-systems are determined, with special attention given to the problems of fringe tracking and dispersion. A concept study for the combination of the VLTI (Very Large Telescope Interferometer) with UVES (UV-Visual Echelle Spectrograph) is carried out, and several other specific instrument pairings are discussed. We show that the proposed combination of an interferometer with a high-resolution spectrograph is indeed feasible with current technology, for a fraction of the cost of building a whole new spectrograph. The impact on the existing instruments and their ongoing programs would be minimal.

S. Albrecht, A. Quirrenbach, R. N. Tubbs & R. Vink

2.1 Introduction

In recent years optical interferometers have proven that they can produce excellent science in the field of stellar and circumstellar astrophysics. Over the same period high resolution spectrographs have enabled the discovery of the first extra-solar planets, and contributed substantially to great progress in the field of asteroseismology.

A number of current interferometric instruments have some spectroscopic capabilities. For example the mid-and near-infrared instruments MIDI (The Mid-Infrared instrument, at the VLTI) and AMBER (Astronomical Multiple BEam Recombiner, at the VLTI) provide spectral resolutions of up to $R \approx 250$ and $R \approx 12000$, over bandpasses of $\approx 5 \ \mu m$ and ≈ 50 nm, respectively. At the CHARA array, the Vega (Visible spEctroGraph and polArimeter) project is under construction with a spectral resolution of $R \approx 30000$ and a bandpass of ≈ 50 nm. For science results obtained with spectrally resolved interferometry see for example Vakili et al. (1998) and Weigelt et al. (2007). Unfortunately the combination of very high spectral resolution over a bandpass greater than a few tens of nanometer, to enable a real analog to classical Echelle spectroscopy with interferometric spatial resolution is not yet available.

In building a dedicated high-resolution Echelle spectrograph for an existing interferometer such as the VLTI, one would face several challenges. First of all, building a high resolution spectrograph is a very costly and time-intensive undertaking. In addition it would be hard to justify building such an instrument only for use with an interferometer, as current optical interferometers are still restricted to very bright objects in comparison with single telescopes. Furthermore, high resolution spectrographs are usually large instruments, while the space available in the beam combining laboratories of interferometers is often limited. Therefore, it is unlikely that such a dedicated instrument will be built in the near future.

In this chapter we advocate a different approach. By using an existing spectrograph and only building an interface between it and an interferometer at the same site, the combination of high spectral and spatial resolution could be achieved on a much shorter timescale, and for a fraction of the cost of a complete new instrument.

The pre-existing infrastructure would need to consist of two telescopes, delay lines for path compensation, a fringe sensing unit to acquire and stabilize the fringes, and a high-resolution spectrograph on the same site. These conditions are already fulfilled, or will be fulfilled in the very near future, at several observatories. The two most promising sites are:

- In the Southern hemisphere at Paranal Observatory with the VLTI in combination with the UVES spectrograph at Unit Telescope 2 (UT2), or the High-Resolution IR Echelle Spectrometer (CRIRES) spectrograph at UT1.

- In the Northern hemisphere at Mauna Kea with the Keck Interferometer (KI) and HIgh Resolution Echelle Spectrometer (HIRES) at Keck I telescope or the NIR-SPEC spectrograph at Keck II. Also at Mauna Kea, the OHANA (Optical Hawaiian Array for Nanoradian Astronomy) interferometer is currently under development, and will allow the combination of several other pairs of telescopes at the Manual Kea site.

In each case, three additional hardware components would be required:

1. A beam combiner that accepts two input beams from the telescopes and feeds the outputs carrying the fringe signals (coded as intensity variations) into fiber feeds;

2. Fibers that connect the interferometer to the spectrograph;

3. A fiber head that feeds the light from the fibers into the spectrograph.

If separate telescopes are available for interferometry (as in the case of the Auxiliary Telescopes of the VLTI), the impact on the single-telescope-use of the spectrograph would be minimal, as it could be used in the interferometric mode during times when other instruments are scheduled for use with the main telescope.

The outline of this chapter is as follows. In Section 2.2 the scientific motivation for the proposed setup will be discussed. Section 2.3 will give an overview of the challenges in designing and building the proposed instrument, and their possible solutions. In Section 2.4 we will give more information about the proposed combination of the VLTI with the UVES spectrograph, and its expected performance. Section 2.5 highlights the main points for other possible interferometer-spectrograph pairings, and Section 2.6 gives our conclusions.

2.2 Scientific case

By taking advantage of the existing infrastructure and instrumentation at the observatories, the proposed interface between a high-resolution spectrograph and an optical / near-infrared interferometer can provide some unparalleled capabilities in a time- and cost-efficient manner. Most importantly, interferometry can be performed with sufficiently high spectral resolution to resolve absorption lines allowing visibility changes across spectral lines to be measured even in late-type stars. The interferometric spectra would also cover a wide wavelength band. Using the broad spectral coverage, one would be able to use cross-correlation techniques to obtain very accurate radial-velocities and line shapes, which have proven extremely helpful in planet search programs and asteroseismology.

Although restricted to observations of relatively bright stars, interferometry at high spectral resolution will provide hitherto inaccessible information on stellar rotation properties, atmospheric structure and surface features, and can have a profound impact on a large number of open questions in stellar astrophysics.

2.2.1 Stellar diameters and limb-darkening

Measuring the variation of the stellar diameter with wavelength, or even better determining wavelength-dependent limb darkening profiles, can provide a sensitive probe for the structure of strongly-extended atmospheres of cool giant stars. Such data can be directly compared with predictions of theoretical models, and provide qualitative new tests of state-of-the-art three-dimensional stellar model atmospheres (Quirrenbach & Aufdenberg 2003). These models make predictions for the emergent spectrum at every point of

the stellar disk. To compare model predictions with data from traditional spectroscopy, they have to be integrated over the full disk first. In contrast, interferometric spectroscopy gives access to the center-to-limb variation of the emergent spectrum, and is thus naturally suited to comparisons with model atmospheres.

A first step in this direction has been made with the Mark III and COAST interferometers and with aperture masking, by measuring the diameters of a sample of cool giant stars in filters centered on deep TiO absorption bands and filters in the nearby continuum (Quirrenbach et al. 1993; Tuthill et al. 1999; Quirrenbach 2001; Young et al. 2003). Many stars are found to be substantially larger in the TiO bands, and to have wavelength-dependent asymmetry. It is easy to understand the principle behind these effects: we effectively measure the diameter of the $\tau = 1$ surface of the star, and the height of that surface varies with opacity and therefore with wavelength. In cool stars this variation may be so large (up to $\sim 10\%$ of the stellar diameter for "normal" giants, even more for pulsating variables) that it can be observed as a variation of the effective stellar diameter with wavelength. The higher parts of the atmospheres are cooler, making the brightness distribution across the stellar surface in absorption bands more sensitive to asymmetries in the temperature distribution. The large spectral widths of the filters used for these interferometric observations average over many TiO absorption lines with different strengths. Interferometric high-resolution spectroscopy will provide much more detailed information on the diameter and limb darkening profiles as a function of TiO absorption depth, and thus substantially better constraints on the theoretical models.

Out of the giant stars which have been observed, the variations of the apparent diameter and limb darkening profile with wavelength are most pronounced in Mira stars. The instrument proposed here will enable detailed investigations of the pulsation and wind acceleration mechanisms. Again, high spectral resolution is required to sample a large range of depths in the stellar atmosphere. The advantage of combining high spatial- and spectral-resolution together in one observation of an object rather than using separate observations in this context has also been pointed out by e.g. Wittkowski et al. (2006); Tsuji (2006).

2.2.2 Interferometric Doppler Imaging

Classical Doppler Imaging (DI) has been developed into a very powerful tool (e.g., Rice 2002; Kochukhov et al. 2004). This technique allows mapping of the chemical and magnetic properties of stellar photospheres with surprisingly small details. Up to now, line profiles have been used for DI which are based on average atmospheric structures; this can obviously only be an approximation, in particular in regions of extreme abundance peculiarity. Tools are now available to compute such stellar atmospheres more accurately (e.g., Shulyak et al. 2004), and a reduced abundance contrast between spots and their surrounding is expected. Interferometric high-resolution spectroscopy data will allow a direct check of the models, because abundance analyses can be performed for individual surface regions of prominent chemically-peculiar stars. The same approach is also applicable for other stars with inhomogeneous surface properties, like active cool giant stars, as interferometry allows the study of individual surface regions. The fact that interferometry can isolate the active regions will partly compensate for the lower total signal-to-noise

compared to single-telescope spectra, which always average over the whole stellar surface.

2.2.3 Pulsations and asteroseismology

Radial and non-radial stellar oscillations also lead to characteristic surface patterns of line shapes and central velocities. The reconstruction of these patterns from line profile variations alone is plagued with ambiguities, however. These can to a large extent be resolved by the additional phase information contained in interferometric data (Jankov et al. 2002). This means that pulsation modes can be identified uniquely without any need for comparisons with theoretical models. Empirical mode identification with interferometric spectroscopy could become an important tool in the field of asteroseismology (Cunha et al. 2007).

2.2.4 Interpretation of radial-velocity variations

Radial-velocity observations of main-sequence stars have yielded more than 250 planet detections so far. The wealth of information from these surveys has revolutionized the field of planetary system physics, but little is known about the incidence of planets around stars with masses higher than about 1.5 $M_\odot$, because more massive main-sequence stars are difficult targets for radial-velocity observations. Surveys of K giants can provide this information, and planets around such stars have indeed been detected (Frink et al. 2002). Planets in highly eccentric orbits can be easily identified as such in high-precision radial-velocity data due to the distinct shape of the Keplerian velocity variations, but sinusoidal variations observed in a number of objects in ongoing radial-velocity surveys of K giants could be due either to planetary companions or to low-order non-radial g-mode pulsations. It is possible in principle to distinguish between these possibilities by analyzing the line shapes (which should vary along with the radial velocity in the case of pulsations, but remain stable in the case of companions), but this requires very high spectral resolution and signal-to-noise. Observations with interferometric spectroscopy could resolve the stellar disk and hence distinguish more easily between these possibilities, which would help to establish the mass function of planets around stars with masses between 3 and 5 $M_\odot$. Similar arguments apply to other cases in which radial-velocity variations could plausibly be attributed to different mechanisms, either related to stellar variability or to companions.

2.2.5 Cepheids

Limb darkening curves measured for a spectral line can provide direct measurements of the projection factors of Cepheid pulsations, which relate the true velocity of the pulsation to the observed radial-velocity curve. Uncertainties in this "p factor", which presently must be computed from theoretical models, are a serious limiting factor in current estimates of Cepheid distances with the Baade-Wesselink method (Sabbey et al. 1995; Marengo et al. 2002; Nardetto et al. 2006). Interferometric spectroscopy can thus elimi-

nate one of the important contributions to the error budget for distances to Cepheids and other variable stars.

2.2.6 Orientation of stellar rotation axes

Stellar rotation induces a difference in the fringe phase between the red wings and the blue wings of stellar absorption lines in resolved interferometric observations. Measuring the position angle of the phase gradient allows determination of the orientation of the stellar axis on the sky (Petrov 1989; Chelli & Petrov 1995). More detailed modeling of the interferometric signal can also provide the inclination of the stellar rotation axis (Domiciano de Souza et al. 2004). High resolution spectroscopy will thus open a way to determine the orientation of stellar rotational axes in space.

To know the orientation of the stellar axes in space is of particular interest in double- or multiple-star systems. One can thus check whether the rotation axes of binaries are aligned with each other, and with the orbital rotation axes of the systems. Here the orientation of the rotational axes contains information about the origin and evolution of the system. Such measurements have only be done for close eclipsing binary systems as one can take advantage of the Rossiter–McLaughlin effect during eclipses (e.g., McLaughlin 1924; Rossiter 1924; Albrecht et al. 2007). However as short-period systems are synchronized early in their life it is important to measure the orientation axes for systems with larger semi-major axes, as they are of fundamental importance for theories of binary star formation. Here the probability that one can observe a eclipse and take advantage of the Rossiter–McLaughlin effect is small.

One can also search for (partial) alignment of rotation axes in star forming regions and stellar clusters. Interactions between stars in multiple systems and other stars in a stellar cluster change the momentum of the systems.

The orientation of the stellar rotation axes will be of special interest for stars which harbor planets, since the mutual inclination between the orbital plane of the companion and the rotation axis of the star can provide insights into the formation and evolution processes of the planet. If the orbital evolution of planetary systems is dominated by few-body scattering processes, or Kozai migration, one might expect to find orbits that are not aligned with the stellar angular momentum (e.g., Lin & Ida 1997; Papaloizou & Terquem 2001; Wu & Murray 2003; Nagasawa et al. 2008). In the near future, astrometric orbits will become available from ground-based and space-based astrometry with the Phase-Referenced Imaging and Micro-arcsecond Astrometry (PRIMA) facility at the VLTI, the Space Interferometry Mission (SIM), and with GAIA. Combining this information with interferometric high resolution observations will provide the relative inclination between the orbital and equatorial plane for a large number of planets in a variety of orbits.

2.2.7 Differential stellar rotation

Along with the oscillation spectrum, differential rotation is a powerful diagnostic for the interior structure of a star. Unfortunately, observations of differential rotation are difficult with classical spectroscopy, and degeneracies exist between inclination, limb darkening,

and differential rotation (e.g., Gray 1977). These degeneracies can be resolved by the additional information from interferometric spectroscopy (Domiciano de Souza et al. 2004). High spectral resolution is of the essence for this application, giving the proposed type of instrument a big advantage over more conventional interferometric spectrographs such as AMBER.

2.2.8 Circumstellar matter

Velocity-resolved interferometric observations of emission lines can be used to determine the structure and velocity field of disks around pre-main-sequence objects and Be stars (e.g., Quirrenbach et al. 1997; Young et al. 2003; Tycner et al. 2006; Meilland et al. 2007). It is possible to determine the disk opening angle and the rotation law in the disk, to measure the location of the inner edge of the disk, and to obtain detailed information on possible asymmetries caused by spiral waves. Interferometric observations of winds and outflows from pre-main-sequence stars and from evolved objects can be used to determine their extent and overall geometry, and to probe sub-structure such as clumps and shells. These observations will not need the full spectral resolution offered by high-resolution optical spectrographs, but access to the Hα line is of critical importance.

2.3 Instrument and infrastructure

In this Section we describe our proposal for combining an optical/IR interferometer with a high resolution spectrograph. Fig. 2.1 shows a schematic drawing of the combined instrument, while a possible design for the beam combiner is shown in Fig. 2.2. Special attention is given to longitudinal dispersion compensation (Section 2.3.2). This has to be addressed if one wants to perform long integrations (several minutes) over a wide bandpass, one of the key abilities of the proposed instrument.

2.3.1 Telescopes

The Earth's atmosphere distorts planar incoming wavefronts from an unresolved astronomical source, introducing phase fluctuations as a function of position and time (Roddier 1981). These fluctuations are commonly described by a Kolmogorov spectrum (Tatarski 1961; Kolmogorov 1941) with constant Fried parameter r_0 (Fried 1966). In order to obtain stable complex visibilities, the incoming stellar wavefronts at the beam combiner have to be flat (with constant wavefront phase as a function of position in the pupil plane for an unresolved star). This can be achieved using either:

1. telescope aperture diameters small enough that the atmospherically-induced phase variations are negligible with $D/r_0 \leq 1$ (this may require a variable pupil stop);

2. tip-tilt correction making wavefront errors negligible on aperture diameters up to $D/r_0 \simeq 3$; or

3. higher-order adaptive optics.

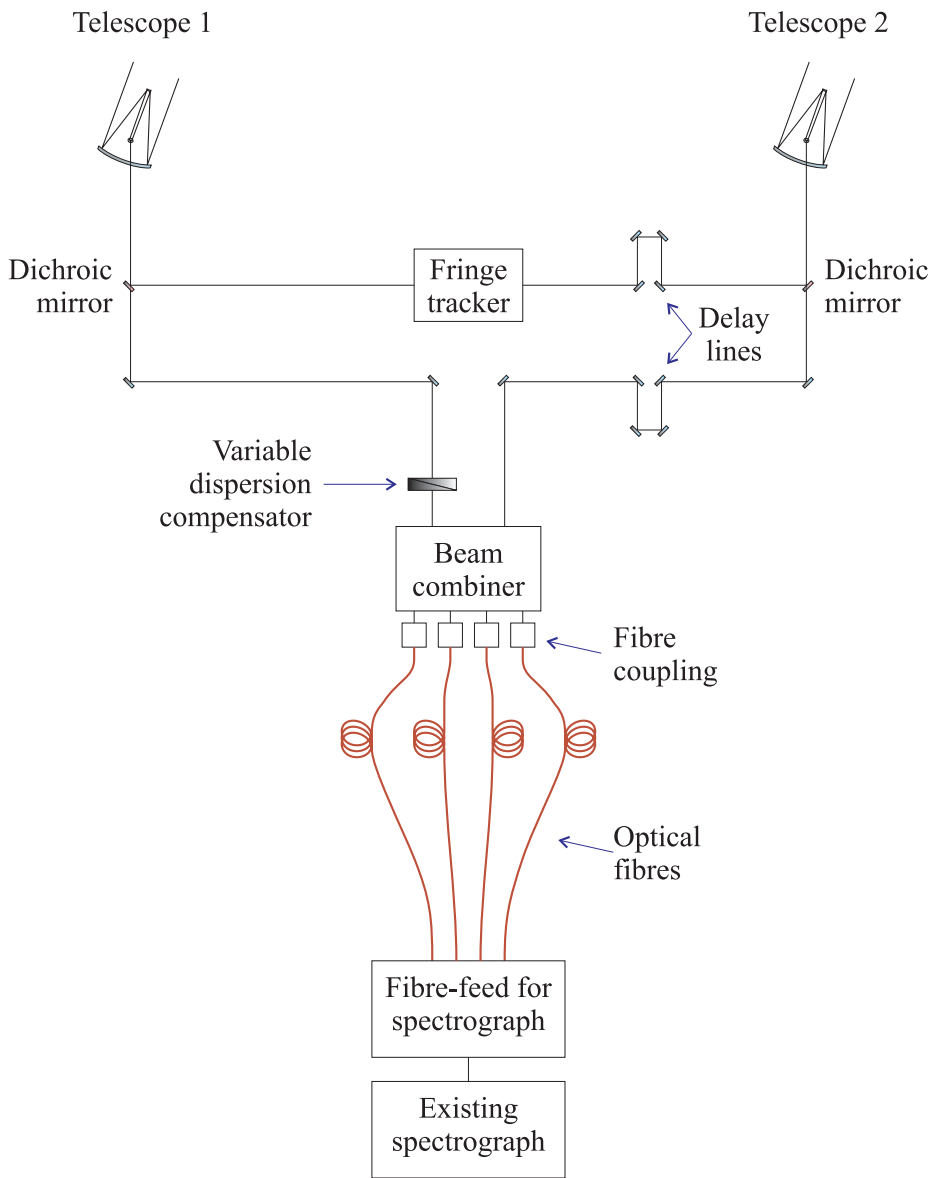Figure 2.1: Schematic of the combined instrument, interferometer and spectrograph. The proposed instrument relies on pre-existing infrastructure (telescopes, fringe-tracker, delay lines and a spectrograph located within a few hundred meters). The additional components which must be built include the variable dispersion compensator, beam combiner, fiber coupling, optical fibers and fiber-feed for the spectrograph.
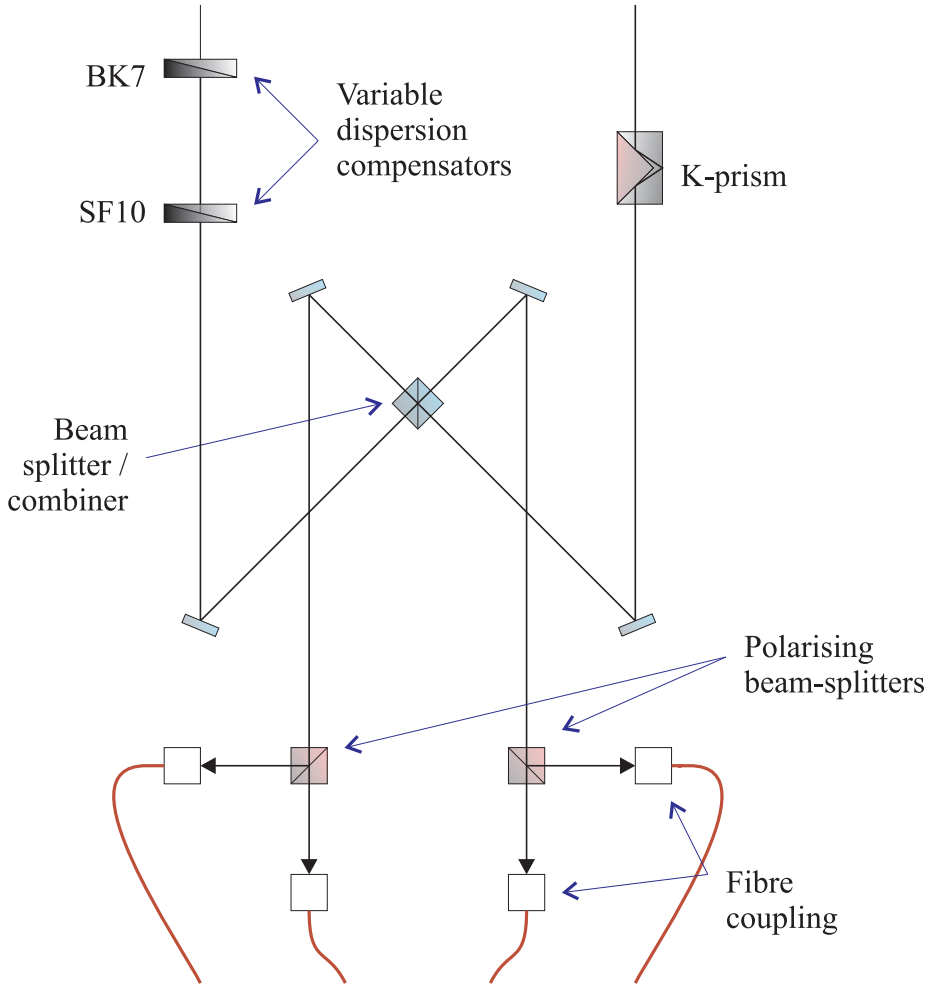
Figure 2.2: Schematic of the suggested beam combiner for the coupling of a spectrograph to an interferometer. The beam from one telescope passes through a K-prism which introduces an achromatic phase shift of $\pi/2$ between the s and p polarizations. The beam from the other telescope passes through longitudinal dispersion compensators. The combination of the two beams in the beam-splitter introduces a phase shift of π between the two output beams. The two polarizations of the two output beams are separated by the polarizing beam-splitters, resulting in four beams with phase relations of 0, $\frac{\pi}{2}$, π, $\frac{3\pi}{2}$ entering the fibers.

Figure 2.3: Change (in m) of OPD during a 10 minute integration as a function of HA and Declination for the G1-J6 AT stations at the VLTI which form a baseline of a length of 192 m and an orientation angle of $-2°$. An angle of $0°$ would indicate a baseline directed towards the North.

Larger apertures can be used at longer wavelengths or under better seeing conditions, as the Fried parameter varies as $r_0 \propto \lambda^{6/5}$ and $r_0 \p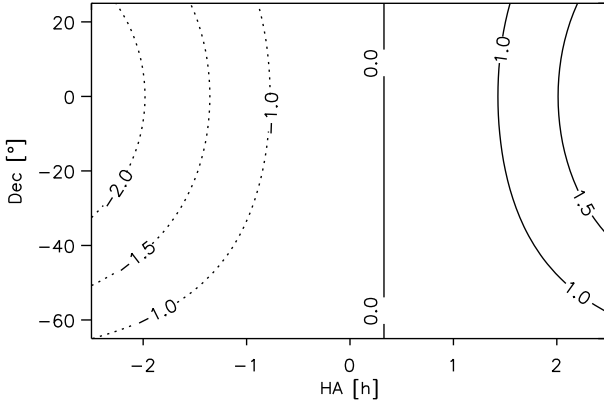ropto 1/\text{FWHM}_{seeing}$ for observations at a wavelength λ and with a seeing disk of FWHM_{seeing}.

2.3.2 Longitudinal dispersion compensation

To compensate for the difference in path length from the two telescopes to the source, optical path must be added to one arm of the interferometer. This is typically achieved through the use of *optical trombone* delay lines or through the stretching of optical fibers (Monnier 2003). If the optical delay compensation is performed in a dispersive medium, the Optical Path Difference (OPD) where the fringes are found will vary with wavelength. Longitudinal dispersion can affect the OPD in the proposed instrument concept in two ways:

1. Dispersion will give a variation of optical delay across the wavelength range of the spectrograph;

2. If the spectrograph operates in a different waveband from the fringe tracker, dispersion will introduce a different OPD in the spectrograph waveband to that in the fringe-tracking waveband.

For a typical high-resolution spectrograph the coherence length of the fringes in each spectral channel is much larger than the optical delay offsets introduced by dispersion. However, time-variation of the dispersion effects during a spectrograph detector integration will blur the interference fringes, reducing the measured visibility amplitude. The two principal sources of variation in optical delay due to dispersion are:

I During an observation the position of the object on the sky changes. To keep the interference fringes at a stable position, the additional optical path introduced in one arm of the interferometer must be varied as the Earth rotates. The change in optical path through the dispersive medium in one arm of the interferometer causes the visibility phase to vary differently at each wavelength. During the course of

Figure 2.4: Same as Fig. 2.3, but this time with a baseline of 109 m length and an angle of 88° (C1-J2).
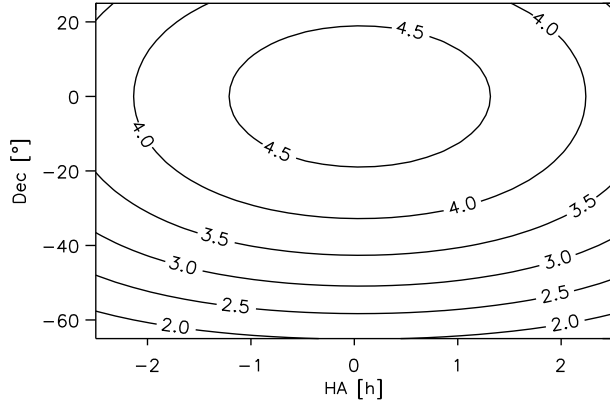
an observation of several minutes this inevitably leads to a loss of fringe contrast for observations in a waveband of non-zero bandwidth. For example, during a 10-minute visible-light integration, the geometric delay path can change by several meters (see Fig. 2.3 and Fig. 2.4), which would lead to a relative OPD shift of several μm between R band and I band.

II A change in the temperature or humidity of the air in one of the optical paths to the star will introduce a change in the column density of air and/or water vapor. To first order, these changes will be corrected by the fringe tracking. The residuals are not expected to be large enough to give different delays for different spectral channels in the spectrograph bandpass. However, if the spectrograph is operating in a different waveband from the fringe tracker, the optical delay in the spectrograph waveband may differ from that in the fringe tracking waveband.

Both dispersion problems could be circumvented by restricting the exposure time, but this would reduce the observational efficiency, and in the read-noise limited regime it would reduce the limiting magnitude. Reducing the spectral bandwidth would solve point I above, but would limit the spectral coverage of the observations. As one can see in Fig. 2.3 and Fig. 2.4, the change in OPD depends on the declination of the star and on the alignment of the baseline with the rotation axis of the earth. Therefore, restricting the baseline geometry and restricting the selection of sources would also circumvent point I above. This would seriously reduce the usefulness of the proposed instrument.

A better way to address point I above would be to equip the beam combiner with a variable atmospheric dispersion compensator (see e.g. Section 2.4.3). This dispersion compensator would correct for the differential dispersion introduced by the few meters of additional path between the two telescopes added during the course of the observations; it does not need to correct for the full differential air path.

Point II can be addressed by estimating the dispersion at the wavelength of the spectrograph using measurements of the ambient environmental conditions (Albrecht et al. 2004) and the variation of optical delay with wavelength across the fringe-tracking bandpass. If the fringe tracker cannot operate sufficiently far from the zero optical group-delay point, then an additional delay line will be required in order to provide a different geometrical

delay for the spectrograph than is used for light that is sent to the fringe tracker, as shown in Fig. 2.1.

2.3.3 Fringe tracker

The proposed instrument scheme relies on the interferometer having a fringe-tracking capability. The fringe tracking must keep the fringes of the spectroscopic observation stable even if they are observed at a different wavelength to the one used for fringe tracking. The fringes in the spectroscopic instrument must be kept stable to a fraction of a wavelength (typically ~ 1 rad of visibility phase). A number of existing interferometers already have fringe-tracking instruments (Delplancke 2003; Colavita et al. 2004; McAlister et al. 2004). The RMS noise (the jitter) in the optical delay from the fringe tracking will cause a reduction in the visibility amplitude by a factor γ:

$$\gamma = \exp\left(-2\left(\frac{\pi\sigma_d}{\lambda}\right)^2\right) \tag{2.1}$$

where σ_d is the RMS variation in the optical delay compensation in a spectral channel with wavelength λ during a detector integration.

2.3.4 Beam Combiner

The primary observable in an interferometer is the complex visibility (having amplitude and phase), proportional to the complex coherence function of the radiation received by the two telescopes (Quirrenbach 2001). The complex visibility can be derived in a number of ways, for example using a fixed delay offset and measuring the fringe signal as a function of wavelength in the spectrum (Labeyrie 1975). Alternatively, to obtain the full information on the complex visibility in each spectral channel, one can measure the four fringe quadratures at each wavelength, i.e. measure the light intensity with fringe phase offsets of 0, $\pi/2$, π and $3\pi/2$ radians. The normalized light intensities as a function of wavelength λ in these four outputs are commonly called $A(\lambda)$, $B(\lambda)$, $C(\lambda)$, and $D(\lambda)$ respectively. The $A(\lambda)$, $B(\lambda)$, $C(\lambda)$, and $D(\lambda)$ outputs can be produced using 50% beam-splitter(s) (providing a π phase shift between the output beams) and achromatic $\pi/2$ phase shifts in two of the four output beams (see e.g. Fig. 2.2). The complex visibility $V(\lambda)$ in the spectral channel at wavelength λ is then fully described by the four intensities $A(\lambda)$, $B(\lambda)$, $C(\lambda)$, and $D(\lambda)$:

$$
\begin{aligned}
V(\lambda) = {} & 2 \cdot \frac{A(\lambda) - C(\lambda)}{A(\lambda) + B(\lambda) + C(\lambda) + D(\lambda)} \\
& + 2i \cdot \frac{B(\lambda) - D(\lambda)}{A(\lambda) + B(\lambda) + C(\lambda) + D(\lambda)},
\end{aligned} \tag{2.2}
$$

where $i = \sqrt{-1}$.

The squared amplitude of this visibility estimate $|V(\lambda)|^2$ and the argument (fringe phase) $\phi(\lambda)$ are given by:

$$|V(\lambda)|^2 = 4 \cdot \frac{(A(\lambda) - C(\lambda))^2 + (B(\lambda) - D(\lambda))^2}{(A(\lambda) + B(\lambda) + C(\lambda) + D(\lambda))^2} \,,$$

$$\phi(\lambda) = \arctan \frac{A(\lambda) - C(\lambda)}{B(\lambda) - D(\lambda)} \,. \tag{2.3}$$

Applying the fringe estimators on a wavelength-by-wavelength basis, one can thus derive the complex visibility as a function of λ.[1]

The absolute phase will usually be corrupted by turbulence in the Earth's atmosphere, but differential phases can be measured between adjacent spectral channels or between the fringe tracking wavelength and one of the observed spectral channels. These differential phases can provide very valuable observables, such as phase differences between the red and blue wings of spectral lines. In sources which are resolved in some spectral lines but which are un-resolved at continuum wavelengths (e.g. Be stars, as discussed in Section 2.2.8), the complex visibilities can be used to make interferometric images of the structure in the spectral lines, using the position of the unresolved continuum source as the phase reference. In this context it is worth noting that phenomena on scales much smaller than the 'resolution limit' λ/B of the interferometer with baseline B are accessible with this technique, because differential phases with a precision of a few degrees provide astrometric accuracy significantly higher than the conventional (imaging) resolution limit.

2.3.5 Connection to the spectrograph

The outputs from the beam combiner can be easily transported to the spectrograph using multi-mode fiber optics. Only the light intensity as a function of wavelength is of interest at this point (after beam combination), so the additional optical path length and longitudinal dispersion from the fiber are unimportant.

For a link at visible or near-infrared wavelengths one could for example use the Optran Plus WF fiber with a core diameter of 100 μm (see Fig. 2.5). Fluoride glass fibers could provide better throughput at longer near-infrared wavelengths.

The insertion of pick-off mirrors might provide a good solution for directing the light from the fibers into the spectrograph. However, in some infrared slit spectrographs, the slit is located in a cryogenic part of the instrument. If it is undesirable to make modifications inside the cryogenic Dewar, it may be sufficient to place the fibers in an image plane outside the spectrograph Dewar.

If the spectrograph is already a fiber-fed instrument, the number of new components will be small and the installation fast.

2.4 An illustrative example: UVES-I

In this Section we investigate in more depth the possible combination of the VLTI interferometer with the UVES spectrograph. We name this combination *UVES-I* in the reminder

---

[1]Note that the estimator for $|V(\lambda)|^2$ in Eqn. 2.3 is biased — $|V(\lambda)|^2$ will be over-estimated in the presence of noise. Slightly modified estimators can be used to give unbiased estimates of $|V(\lambda)|^2$ (e.g., Shao et al. 1988).
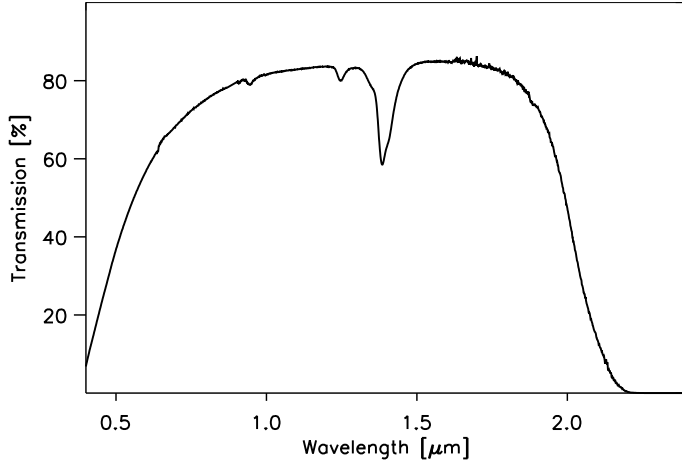
Figure 2.5: Transmission in the wavelength range from 0.4 to 2.5 μm for 150 m of Optran Plus WF fiber (Ceramoptec catalog, see http://www.ceramoptec.com/catalog.htm).

of this chapter. In particular we address here the matter of external fringe tracking and dispersion compensation in Sections 2.4.2 and 2.4.3, respectively. As mentioned above it is essential to solve these points if one wants to combine a high resolution Echelle spectrograph like UVES with an optical interferometer like VLTI and carry out long exposures, which has not been done so far.

2.4.1 VLTI Auxiliary Telescopes

UVES-I would operate in the wavelength range between 0.6 μm and 1.0 μm. Therefore it would use the VLTI ATs (1.8-m Auxiliary Telescopes) and not the UTs (8-m Unit Telescopes) as the Multi Application Curvature Adaptive Optics (MACAO) adaptive optics systems of the UTs do not deliver well-corrected wavefronts in the visible.

The existing tip-tilt correction on the ATs would allow the use of $3r_0$ sub-apertures with UVES-I (corresponding to ~ 75 cm at 800 nm under typical seeing conditions). With the planned installation of adaptive optics systems at the ATs, their full 1.8 m apertures would become useable for UVES-I, corresponding to a sensitivity gain of ~ 2 mag.

The ATs currently have a dichroic beam-splitter sending the visible light to the tip-tilt system, and passing the infrared light to the delay lines and instruments. This beam-splitter reduces the VLTI transmission in the visible considerably (Puech & Gitton 2006). For UVES-I this dichroic should be replaced by 10-90 beam-splitter, with only 10% of the visible light used for tip-tilt correction. The astronomical targets of interest are all bright enough that they will still give good tip-tilt performance. The sensitivity estimates given in Section 2.4.6 are based on this change, and assume a total VLTI transmission of 6% (Puech & Gitton 2006).

2.4.2   Fringe tracking with PRIMA

Starlight at wavelengths longward of 1.5 μm will be separated using a dichroic mirror and sent to the PRIMA fringe tracker (see Fig. 2.2) for stabilization of the fringes. If the R-band fringes at the beam combiner can be stabilized to less than one radian of fringe phase long integrations ($\gg$ than the atmospheric coherence time) can be performed. In order to stabilize the fringe phase at R-band, the OPD at R-band must be calculated from the measured environmental conditions in the VLTI and the measured phases in the PRIMA spectral channels (1.95–2.45 μm).

For the case of von Karman turbulence (Goodman 1985) with finite outer scale L_0, the spatial structure function for the optical phase D_Φ asymptotically approaches a maximum value of $D_\Phi(\infty)$ (Lucke & Young 2007):

$$D_\Phi(r) \equiv \left\langle \left| \Phi(r') - \Phi(r'+r) \right|^2 \right\rangle \to D_\Phi(\infty), \text{ as } r \to \infty \tag{2.4}$$

For von Karman turbulence, Lucke & Young (2007) give a possible range of:

$$0.0971 \left(\frac{L_0}{r_0} \right)^{5/3} < D_\Phi(\infty) < 0.173 \left(\frac{L_0}{r_0} \right)^{5/3} \tag{2.5}$$

The total contribution of seeing to OPD fluctuations is typically estimated by assuming that the seeing is caused by a wind-blown Taylor screen of frozen turbulence passing the interferometer array telescopes at a velocity v (Taylor 1938; Buscher et al. 1995). Under this assumption, the asymptotic value of the temporal structure function will be equal to the asymptotic value of the spatial structure function:

$$D_\Phi(t) \equiv \left\langle \left| \Phi(t') - \Phi(t'+t) \right|^2 \right\rangle \to D_\Phi(\infty), \text{ as } t \to \infty \tag{2.6}$$

For a typical value of $r_0 = 0.25$ m at 800 nm wavelength and $L_0 = 22$ m (Martin et al. 2000) this would lead to a mean-square optical phase variation $D_\Phi(\infty)$ of:

$$170 \text{ radians}^2 < D_\Phi(\infty) < 300 \text{ radians}^2 \tag{2.7}$$

For a two-telescope interferometer with a long baseline, the mean-square variation in fringe phase will be up to twice as large. As this corresponds to fringe motions of several wavelengths, active fringe tracking will be required in order to perform long integrations.

The OPD fluctuations caused by astronomical seeing can be split up into two constituent parts:

1   variations in the mean particle density due to temperature fluctuations (temperature seeing, with no change in the air composition); and

2   replacement of dry air with an equal particle density of water vapor (water vapor seeing, with no change in particle density).
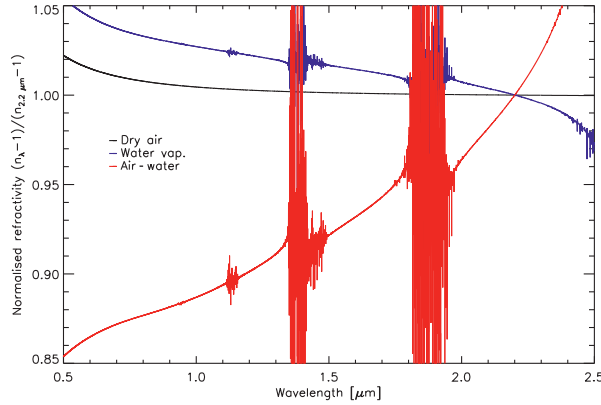
Figure 2.6: Normalized refractivities of air and water vapor, plotted in black and blue respectively. The refractivity (equal to $n-1$ where n is the refractive index) is plotted against wavelength for dry air and water vapor. The refractivity curves have been normalized in this plot such that the refractivity value at 2.2 μm is unity. Also plotted in red is a curve of the refractivity of dry air minus the refractivity of water vapor, which has been normalized in the same way. The normalization process stretches this curve vertically. The data were taken from Ciddor (1996) and Mathar (2004)

Measurements using the MIDI 10 μm instrument at the VLTI indicate that the differential column density of water vapor typically varies by an RMS of $\lesssim 1$ mole m^{-2} (Meisner 2007) due to water vapor seeing (the displacement of dry air by an equal particle density of water vapor). This introduces a mean-square fringe phase fluctuation of up to 50 rad^2 at 800 nm wavelength. The remaining 290–600 rad^2 of mean square phase variation result from temperature seeing[2].

If fringe tracking is performed at K-band, the fringes will be partially stabilized in R-band and I-band. Fig. 2.6 shows plots of the refractivities of dry air and water vapor, normalized to unity at a fringe-tracking wavelength of 2.2 μm. The black *dry air* curve shows the relative amount of OPD at each wavelength if temperature seeing in a dry-air atmosphere introduced 1 unit of OPD at 2.2 μm. For air of finite humidity, the plot of the relative amount of fringe motion would be shifted linearly a small amount ($< 1\%$ of the way) towards the blue *water vapor* curve.

If the geometrical path length is varied in order to stabilize the fringes at K-band against temperature seeing, and no additional compensation is applied to account for the different refractivity in the visible, the correction applied will be 0.5–1.5% too small to stabilize the fringes between 600 and 900 nm. For the 288–602 radians^2 of mean square phase variation expected from temperature seeing, this will lead to an RMS fringe-tracking error of 0.1–0.4 radians at 800 nm wavelength.

The red curve in Fig. 2.6 shows the relative effect of water vapor seeing at different

---

[2]A small fraction of the water vapor column density fluctuations is expected to occur within the VLTI, but this can be ignored when estimating the atmospheric contribution to the temperature seeing.

wavelengths. It corresponds to the difference in refractivity between air and water vapor of the same (low) density, with the curve normalized to be unity at 2.2 μm (the fringe-tracking wavelength). A mean-square fringe phase fluctuation of $\simeq 50$ radians^2 due to water vapor seeing at 800 nm wavelength will correspond to $\simeq 0.90$ μm RMS motion at 800 nm wavelength, but from Fig. 2.6 it can be seen that the fringe motion due to the water vapor seeing will always be 15% larger at 2.2 μm. If K-band fringe tracking is performed with no compensation for the different air refractivity in the visible, this will introduce an RMS residual of $\simeq 1$ radian to the fringe phase at 800 nm wavelength. This would cause a reduction of the fringe visibility due to blurring of the fringes in long exposures.

The approach described by Meisner (2007) for N-band fringe stabilization using PRIMA can be adapted to improve R- and I-band fringe stabilization during fringe phase tracking. In this method, the geometric path from the star and the differential column density of dry air are estimated from the position of the optical delay lines and measurements from environmental sensors in the VLTI (Albrecht et al. 2004). The K-band group phase measurements provided by the PRIMA instrument are only very weakly dependent on the differential column density of dry air, but are strongly dependent on the differential column density of water vapor. If the effect of the estimated dry-air column density is subtracted from the measured group phase, the resulting phase can provide a good estimate of the water vapor column density. The fluctuations in the measured water vapor column density can then be used to calculate and independently correct the residuals produced by water vapor and dry air seeing, assuming that the drift in the geometric delay error is small during one integration.

Analyses of temperature, pressure and absolute humidity data taken on 4 nights immediately following the installation of the four humidity and temperature sensors at Paranal (Albrecht et al. 2004) show that the square root of the temporal structure function of the density of air molecules typically varies by less than 0.003 moles m^{-3} (see Fig. 2.7) at all measured locations within the VLTI, during a 2-minute integration. There is no measurable correlation between the fluctuations in the different ducts to the telescopes and the fluctuations in the main delay tunnel on timescales of a few minutes. The observed water vapor fluctuations within the VLTI are less than 3×10^{-4} moles m^{-3} over a 2-minute integration, and are already included in the $\lesssim 1$ mole m^{-2} figure from Meisner (2007).

In the extremely pessimistic case that all the air in an entire 100-m duct simultaneously undergoes the same 0.003 moles m^{-3} density change, 2 μm of OPD would be introduced at a wavelength of 2.2 μm. The light paths at the VLTI pass through two such ducts and through an air-filled main delay line, but the total OPD fluctuation due to density changes within the VLTI is still expected to be much smaller than the figure of 24–33 μm RMS OPD estimated above for temperature seeing in the atmosphere. The measurements of K-band fringe phase and group phase include the complete path through the atmosphere and instrument as far as the PRIMA optical bench, so OPD fluctuations caused by changes in the ambient conditions within the VLTI will be accurately tracked.

The expected fringe tracking noise introduced by the PRIMA instrument itself will be 100 nm for a star with $m_K = 8$, and 50 nm at $m_K = 6$ (see Figs. 5-12 of Delplancke (2003), and Tubbs et al. (2007)). Equation 2.1 gives visibility losses of 27% and 7.5% respectively at 800 nm, which is easily tolerable.
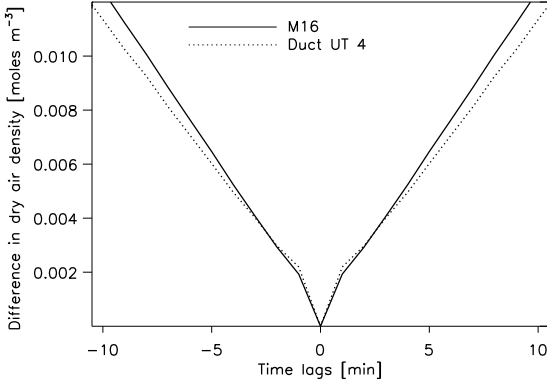
Figure 2.7: Square root of the temporal structure function of the dry air density at two locations in the VLTI for the Night 22/23 September 2004. The solid line shows the temporal structure function for measurements at the M16 mirror in front of the interferometric laboratory, and the dashed line displays the same measurements inside the light duct towards the UT 4 telescope.

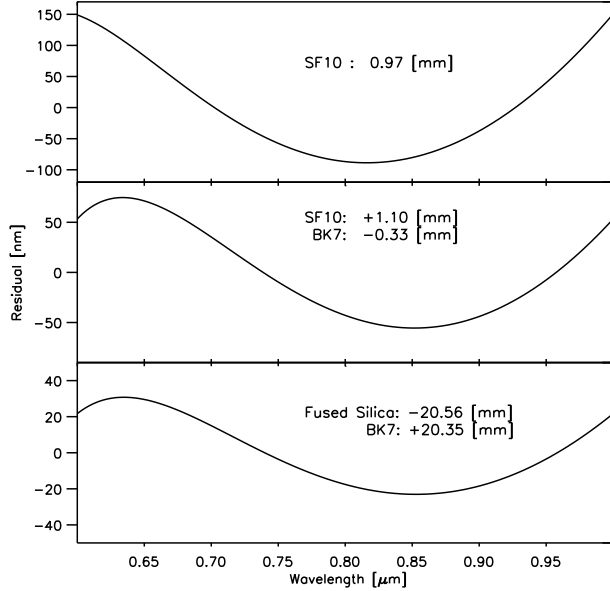### 2.4.3 Dispersion compensation for UVES-I

Each meter of unbalanced air path introduces (under median Paranal atmospheric conditions) offsets from the K-band group delay zero-point of 108 nm and 412 nm, respectively, for the fringes at 900 nm and 600 nm wavelength. This fringe motion can be accurately predicted from environmental sensor measurements and the known geometrical delay. It can be stabilized at one wavelength using a delay line, but to give good stabilization over the full 900 nm to 600 nm wavelength range, a variable dispersion corrector is required.

Starlight at wavelengths shorter than 1.5 μm is separated from the K-band fringe tracking light by a dichroic mirror into the dispersion compensator. The dispersion compensator and the beam combiner are located on the same optical table as PRIMA to ensure alignment and OPD stability (see Fig. 2.2).

Viable solutions for a single-material dispersion compensator exist. Using data from the Schott catalog (http://us.schott.com/sgt/english/products/listing.html), the Sellmeir dispersion formula (e.g. Berger et al. 2003), and Cramer's rule we find that, for the 0.6-μm to 1-μm wavelength range SF10 glass can be used (see Fig. 2.8, upper panel). For extreme parameters — a build up of 10 m delay during integration, compare also to Figs. 2.3 and 2.4 — the residual uncompensated optical path length would reach 150 nm, however; therefore an arrangement where two different materials are used for the dispersion compensation is preferred. A combination of fused silica and BK7 glass gives the best theoretical performance, but the required glass thickness is relatively high (see Fig. 2.8, lower panel). We therefore favor a SF10/BK7 combination, which provides compensation to 70 nm even for extreme delay rates, using much thinner glass elements (see Fig. 2.8, middle panel). The variable dispersion compensator will also compensate for the fixed additional dispersion produced in the K-prism.

In addition to the compensation of the delay differences in the visible band, we must also compensate the delay difference between the visible band and the K-band, where PRIMA tracks the fringes. This can be done by commanding the PRIMA fringe tracker to fringe track far enough from the K-band group delay zero point to allow compensation of the fringes at visible wavelengths, or alternatively by inserting another additional delay as shown in Fig. 2.1.

Figure 2.8: Residual dispersion after accumulation of a 10 *m* change of the total delay, using atmospheric dispersion compensators made of: a] SF10; b] SF10/BK7; and c] BK7/Fused Silica. The combination of SF10 and BK7 (b]) could be used for an instrument like UVES-I. The thickness of the material needed for the compensation is also indicated. For example an additional air path of 10 m in one beam would require the insertion of a 0.97 mm SF10 glass in the other beam.

2.4.4 Beam combiner for UVES-I

One beam is sent through an achromatic phase shifter (e.g. K-prism), which introduces a $\pi/2$ phase shift of one polarization state with respect to the other. Variable dispersion compensation is applied in the other beam. The dispersion introduced by the K-prism is also compensated in the dispersion compensator. Two flat mirrors then direct the beams into the main beam combiner (Fig. 2.2). The combined beams, which have a phase shift of π relative to each other, are sent to polarizing beam-splitters by a second pair of flat folding mirrors (see Fig. 2.2). The polarizing beam-splitters separate the two linear polarizations (with their $\pi/2$ phase differences) giving the four fringe quadratures $A(\lambda)$, $B(\lambda)$, $C(\lambda)$, and $D(\lambda)$.

Full information on the complex visibility can be obtained from the four fringe quadratures $A(\lambda)$, $B(\lambda)$, $C(\lambda)$ and $D(\lambda)$ as discussed in Sect. 2.3.4. For an ideal beam combiner, the complex visibility can then be calculated for each spectral channel using Eqn. 2.2.

The requirements on the precision of the phase shift are rather loose; one can easily tolerate up to $10°$ errors as long as they are stable. Errors in the phase shifts can be compensated for in software, using a similar approach to that used for phase measurements with the PRIMA instrument (Tubbs et al. 2007). Similarly, there are no stringent requirements on the splitting ratios and polarization purity of the beam-splitter cubes. It is therefore possible to mostly use standard commercial components. A preliminary design of the beam combiner fits on a 45 cm ×85 cm breadboard (see Fig. 2.9). This compact design ensures stability and minimizes the space taken up in the beam-combination laboratory of the interferometer. Due to its high spectral resolution, the coherence length of UVES-I is very large ($\geq$ 3 cm). However, the drift of the optical path difference *during* one exposure must not be larger than $\sim$ 50 nm, as this would reduce the fringe visibility due to the fringe
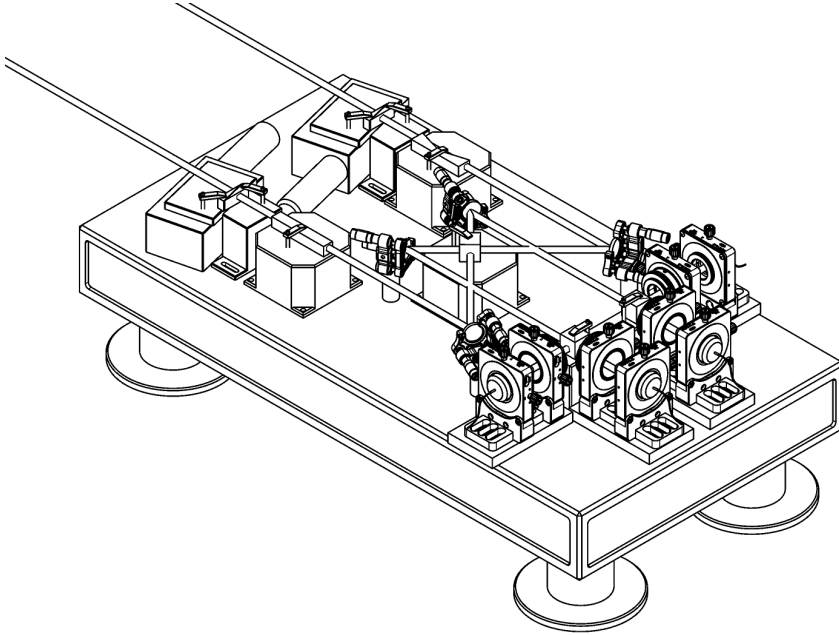
Figure 2.9: UVES-I beam combination table. The light beams from the two telescopes enter from the top left, and pass through the atmospheric dispersion compensator and achromatic phase shifter before being combined at the central beam combiner. The two polarization states are separated, and the resulting four beams coupled into optical fibers; the four fiber holders are visible at the bottom right.

blurring; therefore the UVES-I breadboard should be mounted as rigidly as possible to the fringe sensing unit. This eliminates the necessity of an additional metrology system.

2.4.5 UVES instrument on UT-2

The impact of the proposed combination on the UVES instrument would be small. The UVES-I fiber interface to the spectrograph will be similar to the existing link from FLAMES (Fiber Large Array Multi Element Spectrograph) to UVES (Pasquini et al. 2000), which has a fiber head for 8 fibers. The UVES-I fiber head will be placed after the pre-slit optics and can, when UVES-I is used, be injected via a folding mirror.

To retrieve the full interferometric information only four fibers are needed. It would thus be possible to use two VLTI baselines simultaneously if an eight-fiber feed is used. This would require both of the PRIMA fringe-tracking units to stabilize the fringes on the two baselines. Interesting, but currently not possible at Paranal for a instrument like UVES-I, is the simultaneous use of three baselines, which would make it possible to measure a triangle of baselines, and aquire closure phase. For this a three-way beam combiner, with 12 output fiber is needed and the light from these fibers has to be directed

on the spectrograph CCD with sufficiently-low cross-talk between the different orders.

As the light is injected via fibers into the spectrograph the spectral resolution achieved by the instrument no longer depends on the slit size, but on the core diameter of the fiber and the re-imaging optics. For example using a fiber with a core diameter of 100 μm, the fiber whose transmission is shown in Fig. 2.5, and with re-imaging optics changing the F/3 fiber output beam into the F/10 beam similar to that produced by the standard pre-slit optics of UVES (Dekker et al. 2000), a spectral resolution of $\sim$ 55000 for UVES-I would be achieved, while still making alignment of the fiber-couplers easy.

2.4.6 Performance

The detector integration times used should be sufficiently long to ensure that the detector read-noise is not dominant (see below), and sufficiently short to allow compensation of the atmospheric dispersion accumulating during the exposure with a relatively simple device (see Section 2.3.2). This will typically give exposure times between 1 min and 15 min.

The beam combiner has 12 optical surfaces (before fiber coupling). The transmissive optics will be covered with anti-reflection coatings optimized for the wavelength range used, while mirrors will be coated in protected silver. Using a conservative assumption of 95% efficiency per mirror surface and 99% efficiency per anti-reflection coated glass element, the resulting overall throughput of the beam combination table is 72%.

The transmission of the fiber link depends on the fiber coupling efficiency as well as the bulk transmission losses in the fiber. The fiber link will be similar to the fiber link of FLAMES but the fiber length will be larger –i£¡ about 150 m compared to 40 m for the FLAMES-UVES link. In Fig. 2.5 the transmission for 150 m of Optran Plus WF fiber is given. Note that the transmission changes from 55% to 80% between 0.6 μm and 1.0 μm

Assuming two optical surfaces at each end of the fiber couplers plus one folding mirror which can inject the light into UVES while the spectrograph is in interferometric mode, and the transmission efficiencies described above, the total transmission of the UVES-I link will vary from 45 % to 65 % over the 0.6 μm–1.0 μm wavelength band used.

The system visibility of an interferometer, i.e., the fringe contrast measured on an unresolved source, depends on the wavefront quality of the two beams and on the accuracy of overlap at the beam combiner[3]. Factors influencing the system visibility include alignment, aberrations in the instrument optics, tracking (tip-tilt) errors, and higher-order wavefront errors due to atmospheric seeing. Using tip-tilt corrected $3r_0$ apertures we expect a mean Strehl ratio of $\geq 43\%$ from each telescope (Noll 1976; Fusco & Conan 2004), providing a system visibility of order 0.40.

The total difference in sensitivity between FLAMES and the UVES-I combination depends on the instrument efficiency and the source visibility. The efficiency due to both the throughput and the system visibility would be equivalent to a loss of 10.8 magnitudes (Tab. 2.1) in both the stellar and sky background photon counts. After an integration of 2 min using the maximum spectral resolution and fast read-out rate of UVES-I, one would be in the photon-noise-limited regime for a G0 star of magnitude $R = 6$. In this regime

---

[3]We do not consider the possibility of increasing the system visibility with a spatial filter here, because the introduction of such a filter would impose much more stringent requirements on the alignment and might reduce the fringe temporal stability (Tubbs 2005).

Table 2.1: Comparison of UVES-I throughput with the throughput of UVES-FLAMES, for operation without adaptive optics (0.75 m aperture) and with adaptive optics (full 1.8 m aperture of the ATs).

Term	Flux reduction ($\frac{\text{UVES}-\text{I}}{\text{FLAMES}}$)
Telescope aperture area (no AO / with AO)	0.009 / 0.05
Number of telescopes	2
Transmission VLTI / UT	0.075
Beam combiner transmission	0.72
Fiber link UVES-I / FLAMES	0.75
Flux for real and imaginary components of visibility	0.5
Squared system visibility	0.16
Squared fringe tracking losses	0.85
Total (no AO / with AO)	4.9×10^{-5} / 2.8×10^{-4} 10.8mag / 8.9mag

long integrations can be constructed from multiple short exposures with no additional noise penalty in order to reach the required SNR. The signal-to-noise also varies in proportion to the source visibility. It should be pointed out that even though the sensitivity of UVES-I is significantly lower than that of UVES, the final sensitivity compares quite favorably with other optical interferometers especially bearing in mind that the achieved spectral resolution is very high. The signal-to-noise ratio will be further reduced in proportion to the source visibility, but for many measurements described in Section 2.2 the sources need only be marginally resolved, so that the variation of visibility phase with wavelength directly probes offsets in the position of the emitting region.

For example, for a measurement of the phase change across a spectral line the adjacent continuum provides an excellent calibration, allowing measurement of phase changes with wavelength as small as one milliradian. This means that UVES-I will be sensitive to astrometric offsets that are over one hundred times smaller than the resolution limit of the interferometer. It will not be possible to image such small structures, but models of such astrometric offsets can be constructed and tested with UVES-I.

It should be pointed out that not all observing programs will require the full spectral resolution provided by the new instrument. In those cases it will be possible to obtain a higher SNR per desired spectral element by binning the data. In the readout-noise-limited regime, this can best be done on the CCD. This would have the advantage that one would be able to go to fainter targets than stated above with shorter integration times and shorter

detector readout times.

Often the astrophysical interesting signal is encoded in multiple lines in a spectral region (Section 2.2). In this case the SNR can be improved by cross-correlating these absorption lines with a line-template mask. This is routinely done in high-resolution spectroscopy, (e.g. Griffin 1967; Queloz 1995; Donati et al. 1997; Rucinski 1999) but has not yet been done with optical interferometers, while it would be possible with an instrument like UVES-I.

2.5 Other interferometer-spectrograph pairings

In this section we give some remarks about other possible pairings of interferometers and spectrographs at different sites and in different wavelength regimes.

The high resolution spectrograph CRIRES at Paranal Observatory covers the wavelength range from 1 μm to 5 μm and has a spectral resolution up to $R_{CRIRES} \approx 10^5$ (Kaeufl et al. 2004). The wavelength range would overlap with the wavelength range of AMBER (Petrov et al. 2003) but with a much higher resolution ($R_{AMBER} \approx 12000$). The throughput of the VLTI+CRIRES combination would be higher than UVES-I as the transmission of the VLTI increases towards longer wavelengths. The distortions of the incoming wavefronts are also less severe for the longer wavelengths (see Section 2.3.1), so one would be able to use the full aperture of the ATs or make observations with the UTs using the MACAO AO system (Arsenault et al. 2004). For a combination of CRIRES with the VLTI one could use the Optran Plus WF fiber (Fig. 2.5) as the transmission for a 150 m of Optran Plus WF fiber between 1 μm and 2 μm would be $\approx$ 80 %. Note the dip at $\approx$ 2 μm and the steep decline in transmission beyond 2 μm.

In the Northern hemisphere the Mauna Kea Observatory site would be well-suited for the high spectral resolution optical/IR interferometer design advocated in this chapter. The Keck interferometer (KI) is already in place at the observatory and its infrastructure is similar to the one found at the VLTI (delay lines, 2-μm fringe tracker). The HIRES spectrograph with the spectral range from 0.3 μm to 1.1 μm and a resolving power of $R \approx 67000$ (Vogt et al. 1994) at the Keck I Telescope covers a similar wavelength-range to the UVES spectrograph. Therefore a similar approach as described in Section 2.4 is possible for mating HIRES and KI. The combination of a high resolution spectrograph with an interferometer at this site seems particular attractive from the scientific point of view, as so far the interferometer has no spectrographic mode.

A second interferometer, the OHANA experiment, is also currently being set up at Mauna Kea (Perrin et al. 2004). This instrument uses optical fibers for beam transport instead of the bulk optics used in conventional interferometers. This allows combination of telescopes which were not originally designed for interferometry, forming an array several hundred meters across. Using the OHANA array, one would potentially have access to all spectrographs at the telescopes which are connected to OHANA. However one has to use the bandwidth offered by the OHANA fibers (J,H,K). One would prefer to keep the length of the transport of the beams after the combination in the interferometric lab short to avoid unnecessary losses, therefore one could use the spectrographs at the telescope where the beam combiner is placed. A new beam combiner at CFHT will be

used by the OHANA project in addition to the existing K-band fringe tracker on the Keck Interferometer. The Near Infrared Echelle Spectrograph (NIRSPEC) at the Keck II could be used as the spectrograph.

2.6   Conclusion

This article shows that the combination of high-resolution spectroscopy with long-baseline interferometry gives access to hitherto unobservable properties of stellar surfaces and circumstellar matter.

Furthermore the article shows how this combination can be achieved without building a major new instrument; only a beam combiner and a fiber link are needed. No instrument components are required which would be expensive or time-consuming to make. The use of external fringe tracking is essential for an instrument like this as it enables long integration times. Time-varying longitudinal dispersion could severely limit the possibilities of such an instrument. Dispersion compensation techniques are investigated in this article and a solution is presented which allows integration times up to a few minutes.

The implementation of this approach is shown for the example combination UVES-VLTI. The resulting instrument would differ from other instruments or efforts taken to achieve high spatial and spectral resolution. It would offer spectral resolution nearly a factor 2 higher than for any other interferometric instrument, and over a wide spectral range of a few hundred rather than a few tens of nanometers. It offers the same possibilities to an astronomer as a high resolution Echelle spectrograph behind a single telescope does, plus the high spatial resolution due to the interferometer, albeit only for bright targets. However it is important to realize that this concept, the combination of two existing instruments to create a new one, is not limited to a specific location or instrument, but rather is an approach which can be followed at different observatories in both hemispheres.

It is worth pointing out that the measurements taken with the proposed instruments are differential in nature (e.g. change of visibility amplitude and visibility phase over spectral lines), allowing many interferometric calibration problems to be circumvented. As noted in Section 2.2, these differential measurements contain a wealth of astronomical information in the optical/IR regime.

Acknowledgments

Bibliography

Albrecht, S., Bakker, E. J., de Jong, J. A., et al. 2004, in New Frontiers in Stellar Interferometry, Proceedings of SPIE, ed. W. A. Traub, Vol. 5491, 1266 21, 27

Albrecht, S., Reffert, S., Snellen, I., Quirrenbach, A., & Mitchell, D. S. 2007, A&A, 474, 565 16

Arsenault, R., Donaldson, R., Dupuy, C., et al. 2004, in Advancements in Adaptive Optics. Proceedings of the SPIE, ed. D. Bonaccini Calia, B. L. Ellerbroek, & R. Ragazzoni, Vol. 5490, 47 33

Berger, D. H., ten Brummelaar, T. A., Bagnuolo, Jr., W. G., & McAlister, H. A. 2003, in Interferometry for Optical Astronomy II. Proceedings of the SPIE, ed. W. A. Traub, Vol. 4838, 974 28

Buscher, D. F., Armstrong, J. T., Hummel, C. A., et al. 1995, Appl. Opt., 34, 1081 25

Chelli, A. & Petrov, R. G. 1995, A&AS, 109, 401 16

Ciddor, P. E. 1996, Appl. Opt., 35, 1566 26

Colavita, M. M., Wizinowich, P. L., & Akeson, R. L. 2004, in New Frontiers in Stellar Interferometry, Proceedings of SPIE Volume 5491., ed. W. A. Traub, 454 22

Cunha, M. S., Aerts, C., Christensen-Dalsgaard, J., et al. 2007, A&A Rev., 14, 217 15

Dekker, H., D'Odorico, S., Kaufer, A., Delabre, B., & Kotzlowski, H. 2000, in Proc. SPIE, ed. M. Iye & A. F. Moorwood, Vol. 4008, 534 31

Delplancke, F. 2003, PRIMA, the Phase Referenced Imaging and Microarcsecond Astrometry facility: High Level Requirements & System Description, VLT-SPE-ESO-15700-3051 22, 27

Domiciano de Souza, A., Zorec, J., Jankov, S., et al. 2004, A&A, 418, 781 16, 17

Donati, J.-F., Semel, M., Carter, B. D., Rees, D. E., & Collier Cameron, A. 1997, MN-RAS, 291, 658 33

Fried, D. L. 1966, Optical Society of America Journal, 56, 1372 17

Frink, S., Mitchell, D. S., Quirrenbach, A., et al. 2002, ApJ, 576, 478 15

Fusco, T. & Conan, J.-M. 2004, Journal of the Optical Society of America A, 21, 1277 31

Goodman, J. W. 1985, Statistical Optics, Chapter 8 (Wiley) 25

Gray, D. F. 1977, ApJ, 211, 198 17

Griffin, R. F. 1967, ApJ, 148, 465 33

Jankov, S., Vakili, F., Domiciano de Souza, Jr., A., & Janot-Pacheco, E. 2002, in Astronomical Society of the Pacific Conference Series, Vol. 259, IAU Colloq. 185: Radial and Nonradial Pulsationsn as Probes of Stellar Physics, ed. C. Aerts, T. R. Bedding, & J. Christensen-Dalsgaard, 172 15

Kaeufl, H.-U., Ballester, P., Biereichel, P., et al. 2004, in Ground-based Instrumentation for Astronomy. Proceedings of the SPIE, ed. A. F. M. Moorwood & M. Iye, Vol. 5492, 1218 33

Kochukhov, O., Drake, N. A., Piskunov, N., & de la Reza, R. 2004, A&A, 424, 935 14

Kolmogorov, A. 1941, Akademiia Nauk SSSR Doklady, 30, 301 17

Labeyrie, A. 1975, ApJ, 196, L71 22

Lin, D. N. C. & Ida, S. 1997, ApJ, 477, 781 16

Lucke, R. L. & Young, C. Y. 2007, Appl. Opt., 46, 559 25

Marengo, M., Sasselov, D. D., Karovska, M., Papaliolios, C., & Armstrong, J. T. 2002, ApJ, 567, 1131 15

Martin, F., Conan, R., Tokovinin, A., et al. 2000, A&AS, 144, 39 25

Mathar, R. J. 2004, Appl. Opt., 43, 928 26

McAlister, H. A., Ten Brummelaar, T. A., Aufdenberg, J. P., et al. 2004, in New Frontiers

in Stellar Interferometry, Proceedings of SPIE, ed. W. A. Traub, Vol. 5491, 472 22

McLaughlin, D. B. 1924, ApJ, 60, 22 16

Meilland, A., Stee, P., Vannier, M., et al. 2007, A&A, 464, 59 17

Meisner, J. A. 2007, Using the FSU to generate a phase reference for coherent integration by MIDI at N band, Unpublished 26, 27

Monnier, J. D. 2003, Reports of Progress in Physics, 66, 789 20

Nagasawa, M., Ida, S., & Bessho, T. 2008, ApJ, 678, 498 16

Nardetto, N., Mourard, D., Mathias, P., & Fokin, A. 2006, Memorie della Societa Astronomica Italiana, 77, 235 15

Noll, R. J. 1976, Optical Society of America Journal, 66, 207 31

Papaloizou, J. C. B. & Terquem, C. 2001, MNRAS, 325, 221 16

Pasquini, L., Avila, G., Allaert, E., et al. 2000, in Proc. SPIE, Optical and IR Telescope Instrumentation and Detectors, ed. M. Iye & A. F. Moorwood, Vol. 4008, 129 30

Perrin, G. S., Lai, O., Woillez, J. M., et al. 2004, in New Frontiers in Stellar Interferometry, Proceedings of SPIE, ed. W. A. Traub, Vol. 5491, 391 33

Petrov, R. G. 1989, in NATO ASIC Proc. 274: Diffraction-Limited Imaging with Very Large Telescopes, ed. D. M. Alloin & J.-M. Mariotti, 249 16

Petrov, R. G., Malbet, F., Weigelt, G., et al. 2003, in Interferometry for Optical Astronomy II. Proceedings of the SPIE, ed. W. A. Traub, Vol. 4838, 924 33

Puech, F. & Gitton, P. 2006, Interface Control Document between VLTI and its Instruments, VLT-ICD-ESO-15000-1826 24

Queloz, D. 1995, in IAU Symposium, Vol. 167, New Developments in Array Technology and Applications, ed. A. G. D. Philip, B. Hauck, & A. R. Upgren, 221 33

Quirrenbach, A. 2001, ARA&A, 39, 353 14, 22

Quirrenbach, A. & Aufdenberg, J. 2003, in IAU Symposium, Vol. 210, Modelling of Stellar Atmospheres, ed. N. Piskunov, W. W. Weiss, & D. F. Gray, 68P 13

Quirrenbach, A., Bjorkman, K. S., Bjorkman, J. E., et al. 1997, ApJ, 479, 477 17

Quirrenbach, A., Mozurkewich, D., Armstrong, J. T., Buscher, D. F., & Hummel, C. A. 1993, ApJ, 406, 215 14

Rice, J. B. 2002, Astronomische Nachrichten, 323, 220 14

Roddier, F. 1981, in Progress in optics. Amsterdam, North-Holland Publishing Co., Vol. 19, 281 17

Rossiter, R. A. 1924, ApJ, 60, 15 16

Rucinski, S. 1999, in Astronomical Society of the Pacific Conference Series, Vol. 185, IAU Colloq. 170: Precise Stellar Radial Velocities, ed. J. B. Hearnshaw & C. D. Scarfe, 82 33

Sabbey, C. N., Sasselov, D. D., Fieldus, M. S., et al. 1995, ApJ, 446, 250 15

Shao, M., Colavita, M. M., Hines, B. E., Staelin, D. H., & Hutter, D. J. 1988, A&A, 193, 357 23

Shulyak, D., Tsymbal, V., Ryabchikova, T., Stütz, C., & Weiss, W. W. 2004, A&A, 428, 993 14

Tatarski, V. I. 1961, Wave Propagation in a Turbulent Medium (McGraw-Hill) 17

Taylor, G. I. 1938, in Proceedings of the Royal Society of London A, 164, 476 25

Tsuji, T. 2006, ApJ, 645, 1448 14

Tubbs, R. 2005, Appl. Opt., 44, 6253 31

Tubbs, R. N., Launhardt, R., Meisner, R., & Mathar, R. 2007, ESPRI Exoplanets Search with PRIma: Astrometric Error Budget, VLT-TRE-AOS-15753-0001, V2.1 27, 29

Tuthill, P. G., Haniff, C. A., & Baldwin, J. E. 1999, MNRAS, 306, 353 14

Tycner, C., Gilbreath, G. C., Zavala, R. T., et al. 2006, AJ, 131, 2710 17

Vakili, F., Mourard, D., Stee, P., et al. 1998, A&A, 335, 261 12

Vogt, S. S., Allen, S. L., Bigelow, B. C., et al. 1994, in Proc. SPIE Instrumentation in Astronomy VIII, Volume 2198., ed. D. L. Crawford & E. R. Craine, 362 33

Weigelt, G., Kraus, S., Driebe, T., et al. 2007, A&A, 464, 87 12

Wittkowski, M., Aufdenberg, J. P., Driebe, T., et al. 2006, A&A, 460, 855 14

Wu, Y. & Murray, N. 2003, ApJ, 589, 605 16

Young, J. S., Baldwin, J. E., Basden, A. G., et al. 2003, in Proc. SPIE, Interferometry for Optical Astronomy II, ed. W. A. Traub, Vol. 4838, 369 14, 17

Chapter 4

The spin-axes orbital alignment of both stars within the eclipsing binary system V1143 Cyg using the Rossiter-McLaughlin effect.

The Rossiter–McLaughlin (RM) effect, a rotational effect in eclipsing systems, provides unique insight into the relative orientation of stellar spin axes and orbital axes of eclipsing binary systems.

Our aim is to develop a robust method to analyze the RM effect in an eclipsing system with two nearly equally bright components. This gives access to the orientation of the stellar rotation axes and may shed light on questions of binary formation and evolution. For example, a misalignment between the spin axes and the angular momentum of the system could bring the observed and theoretical apsidal motion into better agreement for some systems, including V1143 Cyg.

High-resolution spectra have been obtained both out of eclipse and during the primary and secondary eclipses in the V1143 Cyg system using the 0.6 m Coudé Auxiliary Telescope (CAT) and the Hamilton high-resolution spectrograph at the Lick Observatory. The Rossiter–McLaughlin effect is analyzed in two ways: (1) by measuring the shift of the line center of gravity during different phases of the eclipses and (2) by analysis of the line shape change of the rotational broadening function during eclipses.

We measured the projection of the stellar rotation axes using the rotation effect for both main-sequence stars in an eclipsing binary system. The projected axes of both stars are aligned with the orbital spin within the observational uncertainties, with the angle of the primary rotation axis $\beta_p = 0.3 \pm 1.5°$, and the angle of the secondary rotation axis $\beta_s = -1.2 \pm 1.6°$, thereby showing that the remaining difference between the theoretical and observed apsidal motion for this system is not due to a misalignment of the stellar rotation axes. Both methods utilized in this paper work very well, even at times when the broadening profiles of the two stars overlap.

S. Albrecht, S. Reffert, I. Snellen, A. Quirrenbach & D. S. Mitchell

HIP	96620	
R.A.$_{J2000}$	$19^h38^m41^s$	‡
Dec.$_{J2000}$	$54°58'26''$	‡
Parallax	$0.''02512(56)$	‡
V$_{max}$	5.89 mag	‡
Sp. Type	F 5 V	†
Period	$7.^d6407568(6)$	⋆
Inclination	$87.0(1)°$	†
Radius$_p$	$1.346(23)R_\odot$	†
Radius$_s$	$1.323(23)R_\odot$	†
L$_s$/L$_p$	0.96(3)	†

Table 4.1: Parameters for V1143 Cyg taken from ESA (1997)‡, Andersen et al. (1987)† and Giménez & Margrave (1985)⋆. Radius$_p$ denotes the radius of the primary component and Radius$_s$ the radius of the secondary component. L_s/L_p denotes the luminosity ratio between the secondary and primary.

4.1 Introduction

Eclipsing binaries are great stellar laboratories for gathering information on stellar surface structure. During eclipses, varying parts of the stellar disk are obscured, allowing the observer to gather spatially resolved information. Without eclipses, this information is hardly accessible.

The crossing of a companion in front of a rotating star causes a change in the line profile of the eclipsed star as, for example, it first covers mainly the part of the stellar surface which is moving towards the observer. This change in the line profile results in a change in the center of gravity of the line and therefore in a change in the measured radial-velocity of the star. The strength and shape of this rotation effect is a function of the projection of the stellar axes on the sky, its inclination (for stars with differential rotation), the projected rotational velocity, the stellar radius, the radius of the companion, the stellar limb darkening, and the orbital parameters of the system.

The rotation effect was first observed by Rossiter (1924) in β Lyrae, and by McLaughlin (1924) in the Algol system. The theory of the rotation effect is well understood (e.g. Kopal 1959, Hosokawa 1953, Ohta et al. 2005, and Giménez 2006). In contrast, observations of the rotation effect in eclipsing binary systems are rare (e.g. Hube & Couch 1982 and Worek 1996). Observation and analysis of the RM effect has recently received renewed interest, caused by the possibility of observing the spin-orbital alignment for transiting exoplanet systems (e.g. Queloz et al. 2000 and Winn et al. 2006) and the potential to observe features of the planetary atmosphere (Snellen 2004).

For the successful observation and interpretation of the rotation effect in a planetary system, the required S/N and precision in radial velocity are significantly higher than those required to analyze the RM effect in a stellar binary system. However, the difficulty in analyzing a stellar binary system lies in the fact that one has to deal with the additional light from the eclipsing foreground star. The spectral lines of the two stars normally blend during the eclipses, which makes an analysis of the rotation effect in the framework of the change of the center of gravity during an eclipse difficult. Nevertheless, the observation of the rotation effect is of astrophysical interest in binary systems, as it might reveal the orientation of the stellar rotation axes and provide information about stellar surface
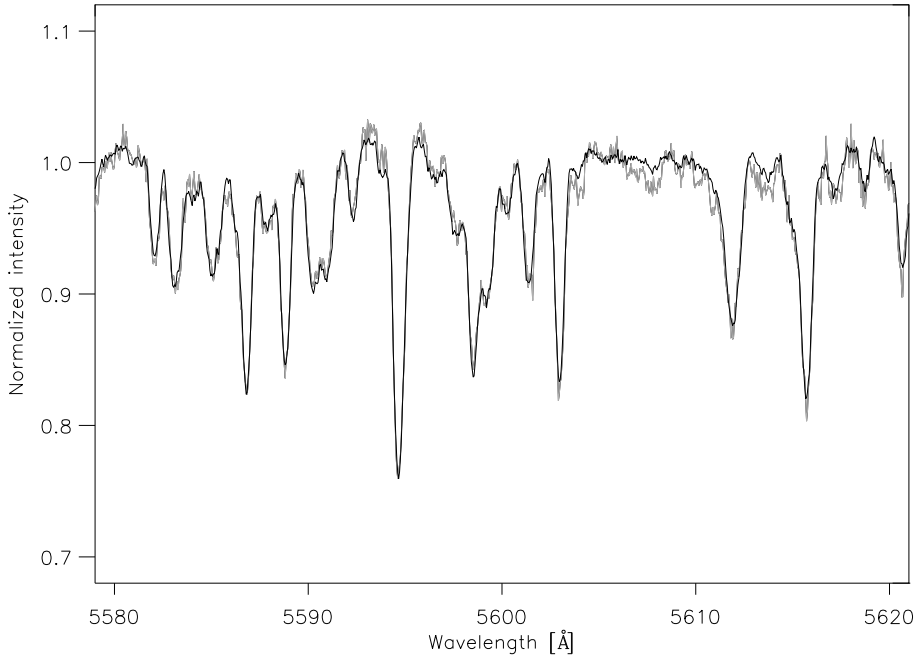
Figure 4.1: Normalized spectrum of V1143 Cyg covering the wavelength range from 5580 to 5620 Å. The thin line represents the spectrum, and the thick line represents the convolution of the narrow-lined template with the BF obtained using the SVD algorithm. The quality of the representation of the spectrum by the BF and the template is also typical for other wavelength regions.

velocity fields. The knowledge of these quantities might help to answer questions related to binary formation and evolution, and to the study of apsidal motion.

Accordingly, our aim in this research is twofold: I) to develop a method tfor deriving information about the orientation of the stellar rotation axes in an eclipsing system with two nearly equally bright components; II) to apply it to an astrophysically interesting system, V1143 Cyg (e.g. Andersen et al. 1987; Giménez & Margrave 1985). V1143 Cyg (Table 4.1) is a bright system consisting of two F5V stars, and has a high eccentricity ($e = 0.54$) that makes it an ideal candidate for testing a new algorithm. Because of the high eccentricity, the spectral lines are not as extensively blended during eclipses. V1143 Cyg is a young ($2 \cdot 10^9$ yr) system (Andersen et al. 1987), and the measured apsidal motion, i.e. the precession of the orbit in its own plane ($0.000705\pm0.000041°$/cycle, Giménez & Margrave 1985), is only marginally compatible with what is expected theoretically ($0.00089\pm0.00015°$/cycle, Andersen et al. 1987). The precession of the periastron is caused by a general relativistic effect and a Newtonian contribution, the latter consisting of two terms which are due to the deformation of the two stars by tides and stellar rotation. Andersen et al. (1987) suggested the possibility that it could be possible that the tidal
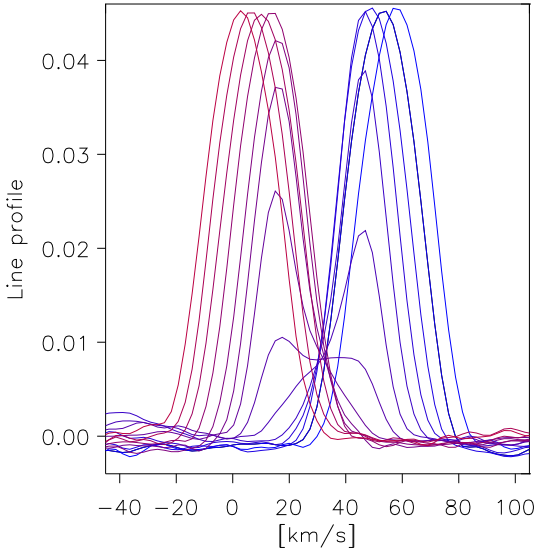
Figure 4.2: The panel shows two BFs obtained shortly before (higher radial-velocities), nine during, and two after the primary eclipse (lower radial-velocities), with the secondary BF subtracted, in velocity space. One can see how the part of the stellar disk which is moving towards the observer is initially obscured. Later in the eclipse a more central part of the stellar disk is covered while at the end of the eclipse parts of the disk that emit red-shifted light due to the rotation are covered. Note that the BF of the primary is moving through velocity space. These observations were obtained at ≈ 30 min intervals.

evolution has not yet achieved parallel rotation axes of the stars and the orbit. This would reduce the expected apsidal motion, thereby bringing it into a better agreement with the measured apsidal motion.

In the following section we present our observations. Section 4.3 describes the data reduction and the two methods used to derive the orbital and stellar parameters. The results are discussed in Section 4.4. A summary is given in Section 4.5.

4.2 Observations

V1143 Cyg was observed in the summer/autumn of 2005 and 2006 with the 0.6 m CAT telescope at the Lick observatory, equipped with the high-resolution Hamilton Echelle Spectrograph. Observations of the primary eclipse (≈ 4 hours) were made on the night of August 29/30, 2005 with two observations before, nine observations during, and four observations after the eclipse. The central part of the secondary eclipse (≈ 8 hours) was observed during the nights August 04/05 and 27/28, 2005. In addition, another 20 observations were made out of eclipse in order to obtain an accurate orbit model. During each night, we also observed a set of different radial velocity standard stars. Before and after every exposure of V1143 Cyg (≈ 20 min) or a standard star, we made a Thorium-Argon (ThAr) exposure to obtain a wavelength scale taken close in time to the observation, minimizing the influence of drifts in the spectrograph on our measurements. Data from the secondary eclipse taken on August 27/28 had to be discarded from the final analysis, because of an erroneous ThAr wavelength calibration during that night.

Figure 4.3: The same as Fig. 4.2 but for the secondary eclipse. One can see BFs of the eleven observations obtained during the secondary eclipse with the line profile of the primary subtracted. The change in radial-velocity during the secondary eclipse is smaller than during the primary eclipse also, the coverage of the secondary is less than the coverage of the primary during its eclipse. This is due to the orbital inclination not being 90°, and the greater distance between the two stars along the line of sight during secondary eclipse (See Fig. 4.5).
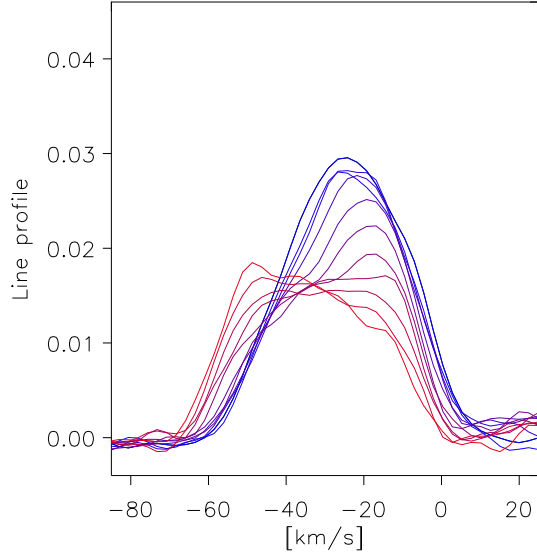
4.3 Analysis and results

For our analysis we used a wavelength range from 4430 Å to 5750 Å, excluding the regions with telluric lines, Hβ, and areas for which an insufficient continuum correction was achieved in the spectra (usually the edges of the orders). The first steps of the data reduction consisted of bad-pixel exclusion and continuum normalization. The latter was carried out by fitting a polynomial of 5th order to the spectra and subsequently dividing the spectra by it.

In the next step, a weighted mean of the two wavelength scales, based on the two ThAr spectra obtained directly before and after each observation, was constructed. The weighting took into account time differences of the photon weighted midpoint of the observation and the times of the ThAr exposures. The resulting error in the calculated radial-velocity due to the drift of the spectrograph during the observation was estimated to be 75 m/s on the basis of comparisons of several ThAr exposure pairs.

The Broadening Function (BF) was calculated to retrieve the line profiles of the two stars, governed by the velocity fields on the stellar surface and stellar rotation. The BF represents the function that projects a narrow-lined template onto the broadened spectrum. We calculated the BF using the singular value decomposition (SVD) technique. This approach is clearly described in Rucinski (1999), whereas the SVD algorithm itself can be found in Press et al. (1992).[1] In order to calculate the BF one needs a narrow-lined template; we used the spectrum of the F7V star HD 222368 (Udry et al. 1999), obtained as one of the radial-velocity standard stars. Before using the spectrum of HD 222368 as a narrow-lined template we deconvolved it using the maximum-likelihood method in

---

[1]We took all singular values until the first derivation of the difference between the observed spectrum and template broadened by the BF with respect to the singular values used for the calculation of the BF effectively reached zero.

conjunction with a kernel calculated with the same code as applied in Section 4.3.2. An iterative approach was used to identify the kernel that gave the best results. The most satisfactory results are achieved when using a kernel with a projected rotational velocity (*vsini*) of 5 km/s. Figure 4.1 shows a part of a typical spectrum obtained from the V1143 Cyg system. It also shows for comparison the convolution of the narrow-lined template with the BF. As V1143 Cyg is a double-lined binary system with two components of the same spectral type, the BF itself consists of two peaks that represent the broadening functions of the two stars, shaped by the corresponding rotation and velocity fields.

In this study we are primarily interested in the data taken during the eclipses and their interpretation in the framework of the RM effect. Because of the high eccentricity ($e = 0.54$) of the system, the midpoints of the eclipses do not occur when the radial-velocities of the stars are equal, but shortly before and after the time of equal velocity, for the primary and secondary eclipses, respectively. During the middle and the end of the primary eclipse the lines of the two stars are blended. The same situation occurs during the beginning and the middle of the secondary eclipse. Hence, although the line blending is not as severe as in the case of a circular orbit, the light from the foreground star cannot be ignored.

We followed two different approaches to derive the spin axis of the eclipsed star with blended lines. The first method is explained in Section 4.3.1. We first show how the influence of the foreground star is subtracted, and subsequently how the center of gravity from the BF of the eclipsed star is calculated. In Section 4.3.2 the BFs of *both* stars are used. Here we do not use the center of gravity of the measured BFs to derive the RM effect, but the shape of the BFs and their change during the eclipse. The measured BFs are compared to simulated BFs, and thereby the parameters that govern the rotation effect are derived.

4.3.1   Method 1: The BF's center

Before determining the parameters involved in the RM effect, an orbital model has to be obtained. To derive the radial-velocities of the components out of eclipse, we fitted two Gaussians to the two peaks in the BFs. A χ^2 fit was applied to extract the orbital parameters. In this work, we adopted the orbital period ($7\overset{d}{.}6407568 \pm 6 \times 10^{-7}$) for all fits, since it is derived at much higher accuracy from eclipse photometry than from radial-velocity variations (Giménez & Margrave 1985). The inclination of the orbit ($87.0 \pm 0.1°$), and the sizes of the components $1.346 \pm 0.023 R_\odot$ and $1.323 \pm 0.023 R_\odot$ have been adopted from Andersen et al. (1987); these are needed for later analysis. The fitted parameters are shown in the second column of Table 4.2 with their 1-σ uncertainties. In addition, the orbital parameters given by Andersen et al. (1987) and Giménez & Margrave (1985) are shown for comparison in column five.

Figure 4.5: The orbit of the binary system V1143 Cyg shown from above the orbital plane. The solid line represents the orbit of the primary component and the dashed line the orbit of the secondary. The lines from the center of gravity towards the orbits indicate the position of the periastron. The big dots indicate the positions of the stars at time of mid primary eclipse.
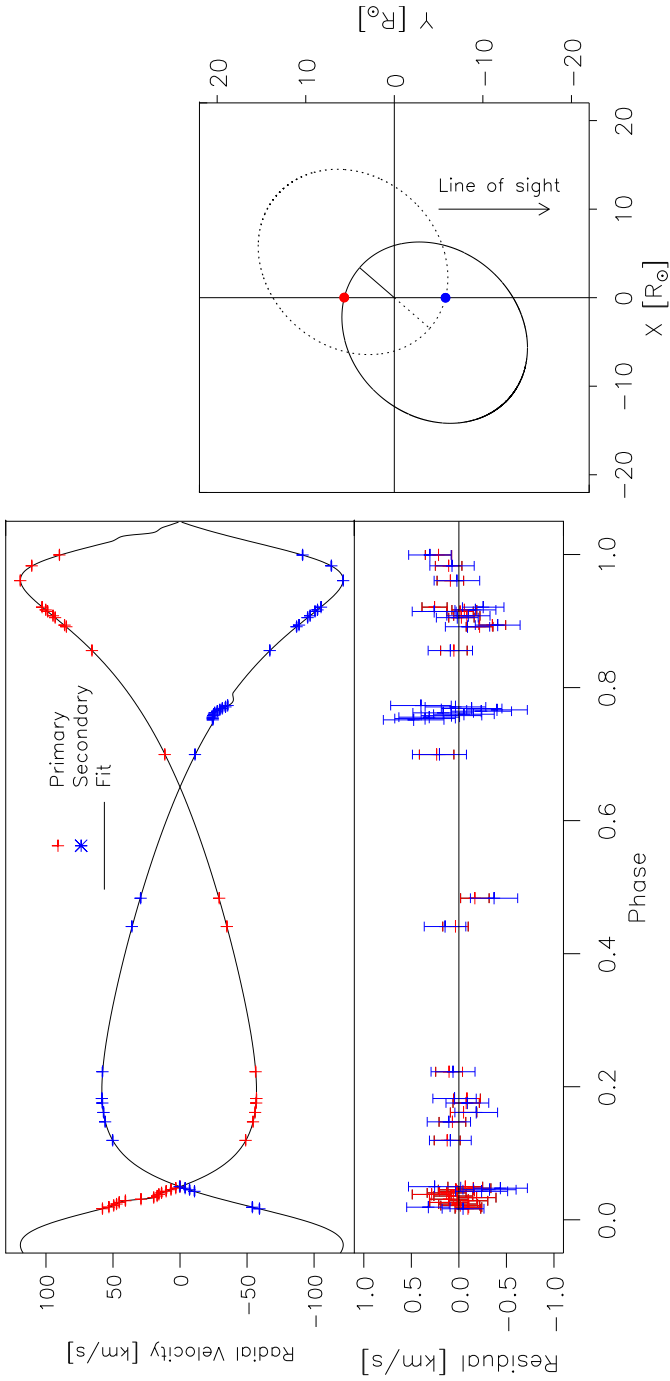
Figure 4.4: The radial-velocity measurements of the primary and secondary components of V1143 Cyg, and the orbital solution, are plotted against orbital phase. The lower panel shows the difference between the best fit and the actual measurements of the radial-velocities of the primary and secondary component. The midpoint of the primary eclipse occurs at a phase of ≈ 0.03, and the midpoint of the secondary eclipse at a phase of ≈ 0.77. Please note that the systemic velocity in this graph and in Figs. 4.6 and 4.7 is already subtracted
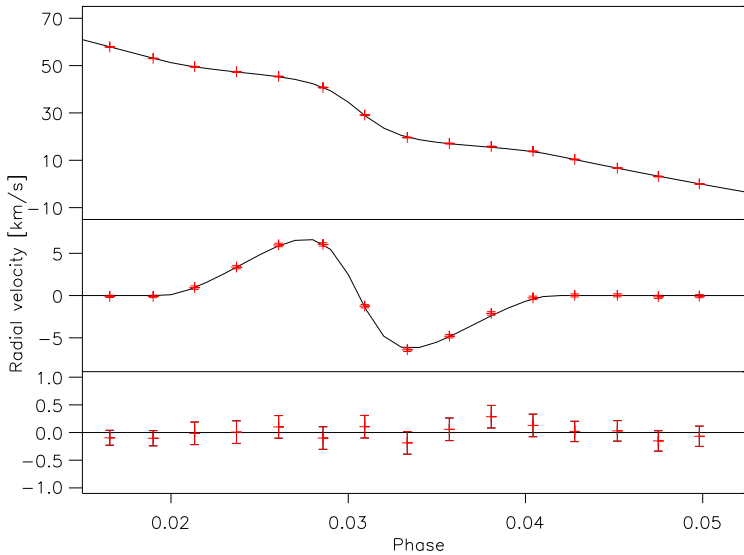
Figure 4.6:   The rotation effect during the primary eclipse. The shift of the center of gravity is plotted against the orbital phase. The upper panel shows the measured radial velocities along with the best fit. In the second panel the radial velocity due to the orbital motion is subtracted from the data and the fit. The residuals between data and fit are shown in the third panel.

The tomography algorithm of Bagnuolo & Gies (1991) is used to disentangle the primary and secondary spectra. This algorithm uses, the spectra obtained at different phases of the orbit, and the orbital parameters of the system, as input. It starts with two synthetic spectra without spectral lines for the two components in V1143 Cyg. For all observations taken outside the eclipses, it shifts the observed spectra in the rest-frames of each component using the newly obtained orbital parameters. Subsequently, the synthetic spectra are compared with the observed spectra. The mean of all the differences between the synthetic and observed spectra is added to the synthetic spectra. This complete process is repeated 50 times, but in our case it converged after only a few iterations.

In the next step, the spectrum of the foreground star is subtracted. For an observation out of eclipse this is straightforward, using the spectrum shifted in velocity space to the appropriate position. During eclipses, one has to incorporate the change in the light ratio of the two stars due to the eclipses. For this we assumed a linear limb darkening law with a limb-darkening coefficient (u) of 0.6 for both stars. Subsequently, the BF was calculated with only one star in the spectrum. Figures 4.2 and 4.3 show the BFs of the primary and secondary stars during their eclipses, after subtraction of the foreground star. Note that, for computational reasons, the continua of the observed spectra were set to zero and the signs of the spectra have been changed; this results in positive BFs.
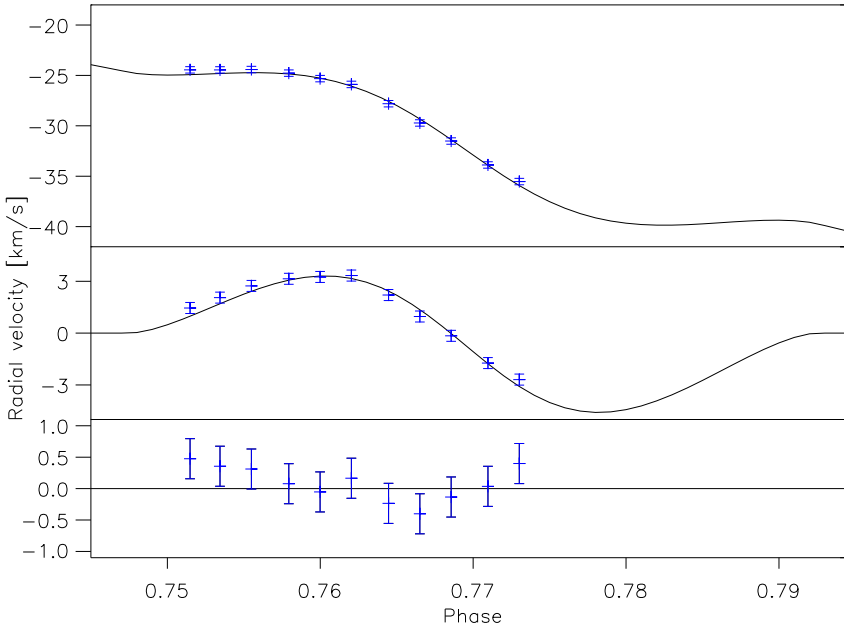
Figure 4.7: The same as for Fig. 4.6 but this time for the secondary eclipse.

The center of gravity of the absorption lines can now be extracted from the BFs and used to calculate the radial-velocity of the eclipsed star, including the radial-velocity anomaly introduced by the RM effect. Using the orbital model and the formula by Kopal (1959) and Hosokawa (1953)[2] to calculate the rotation anomaly, the orbital parameters and the parameters relevant for the RM effect of the two stars can be derived jointly with a χ^2 minimization algorithm; therefore *vsini* and the angles β_p and β_s enter as new parameters. β is the angle between the stellar spin axis projected onto the plane of the sky and the orbital spin axis projected onto the plane of the sky. $\beta = 0°$ would indicate a projected rotation axis perpendicular to the orbital plane, whereas $\beta = 90°$ would indicate that the rotation axis lies in the orbital plane. The longitude of the ascending node of the orbit (Ω) is not known, resulting in an ambiguity in the sign of the angle β. In our definition, a positive β indicates that the RM-effect, integrated over the complete eclipse, would give a positive residual in radial-velocity. The companion passes over a larger stellar surface area which is moving towards the observer than over surface area which is moving away from the observer. The linear limb-darkening coefficients of both stars are fixed during the fits to 0.6 as they are only weakly constrained by our fits. In the χ^2 fit, all data points out of eclipse and all data points during the primary and secondary eclipses are fitted simultaneously. Our radial-velocity data points, the best, fit can be seen in Fig. 4.4 for the complete orbit including the two eclipses. Figure 4.5 shows the orbit from a point above the orbital plane. Figures 4.6 and 4.7 display the radial-velocities of the primary

---

[2]Equation 5 has to be adopted for eccentric orbits.

and secondary stars during and around their eclipses. The best fit parameters are listed in the third column of Table 4.2 with their 1-σ uncertainties, as derived from the χ^2 fit. All radial-velocity measurements are given with their epochs in Table 4.3 in the Appendix. The radial-velocities directly after the primary eclipse, and the data point at a phase of 0.7, have been extracted using a Gaussian fit to the BF of one star after the subtraction of the other star in the spectrum; however, there is no significant change in the derived parameters if these data points are omitted. The average uncertainties in the radial-velocities, out of the eclipses, are 0.15 km/s for the primary and 0.25 km/s for the secondary. The uncertainties of those radial-velocity measurements that were determined from the centers of the lines, we estimated to be 0.20 km/s for the primary and 0.32 km/s for the secondary. This was calculated by comparing them with the velocities obtained from a Gaussian fit outside the eclipses.

4.3.2   Method 2: Variation of the BF profile

In our second approach, to derive information about the binary orbit and the orientation of the rotation axes, we simulated the shape of the BF of the two stars, as governed by the orbital motion, stellar rotation, orientation of the stellar spin axes, velocity fields on the stellar surface, limb-darkening and, in case of a measurement taken during an eclipse, the fraction of the stellar disk which is covered by the companion at the time of the measurement. These simulated BFs were subsequently compared to the measured BFs, and the relevant parameters determined. With this method, we not only use the first moment of the stellar absorption lines during the analysis, but we utilize the complete BF and its change over the course of the eclipse as a diagnostic tool for determining the orbital and stellar parameters.

We simulated the rotation profile of the two stars in the V1143 Cyg system with a few thousand elements across the visible half-spheres with equal surface brightness. We included linear limb-darkening, asymmetric macro-turbulence and solar-like differential rotation (See Gray 2005). Accordingly, besides the parameters which were fitted in Section 4.3.1, another parameter, the Gaussian width of the macro-turbulence, is required. We kept the σ of the Gaussian for the tangential and radial-velocity fields ζ_{RT} and their covered surface fraction equal, as the quality of the fit did not improve by including them as free parameters. The inclination of the orbit and the sizes of the two stars can be varied in our fits. However, in the final fits presented here, we used a linear limb-darkening coefficient of 0.6, solid body rotation, and the inclination and radii from the literature (see also Section 4.4).

Each exposure of V1143 Cyg had a duration of ≈ 20 min. Provided that one takes the photon midpoint of the observation, this poses no serious problem for the analysis of the center of gravity of the lines. However, looking at the line profile, one has to take two effects into account. First, the radial-velocities of the two stars change during a 20-min exposure. This effect is strongest in our data set at the time of the primary eclipse, where the change in radial-velocity is ≈ 3 km/s during one exposure. This artificially widens a BF taken during a 20 min exposure relative to a BF which would have been taken instantaneously. During the eclipses, a second effect becomes important; the coverage of the eclipsed stars can change considerably during 20-min. Again, this effect is stronger

during the primary eclipse than during the secondary eclipse, as the primary eclipse is deeper and shorter. Sine we need an exposure over several minutes to receive a sufficiently high S/N ratio[3], we introduced the same 'smearing' in the simulated BFs. We calculated three BFs for each exposure and stacked them together: one simulated observation 6.6 minutes before the photon midpoint, one at the photon midpoint and one 6.6 minutes after the photon midpoint. We convolved each simulated BF with a Gaussian of $\sigma = 2.5$ km/s, representing roughly the resolution of the spectrograph in the wavelength range used.

In addition to the parameters describing the binary system, one parameter is included that scales all simulated BFs to the observed BFs. The primary star has a slightly higher luminosity than the secondary. Also, the template used might fit one of the two stars better than the other one. Therefore, we included another parameter scaling the height of the kernels of the two stars relative to each other. As mentioned in the beginning of this section, all spectra have been normalized. During the eclipses the absolute amount of light changes. Hence the depths of the absorption lines change relative to the normalized continuum, and therefore the height of the BFs also change. This has to be incorporated in the calculations of the BFs. We performed a fit using all 46 spectra obtained out of eclipse and during the primary and secondary eclipses. The derived values for the parameters are given in column four of Table 4.2. The measured BFs and the best fits can be seen in Fig. 4.8 for the primary eclipse and in Fig. 4.9 for the secondary eclipse. The uncertainties were calculated using the bootstrap method described in Press et al. (1992).

4.4 Discussion

4.4.1 Orbital parameters

Using the methods described in Section 4.3.1 and Section 4.3.2 we obtained values for the orbital parameters of V1143 Cyg and for the stellar parameters of the two stars. The time of periastron passage of the primary (T), the longitude of the periastron (ω), and the eccentricity (e) were determined in all three fits, and agree with each other to within the 1-σ level. Using the values from Giménez & Margrave (1985) for ω (48.26 $\pm$ 0.01°) and the apsidal motion rate (0.000705$\pm$0.000041°/cycle), and taking the time difference into account, one would derive an ω of 49.31° $\pm$ 0.06° for the time of our observations. This is also the value stated in Table 4.2. The parameter for the semi-amplitude of the secondary (K_s) (90.0 $\pm$ 0.1 km/s) falls outside the 1-σ range of the literature value (91.1 $\pm$ 0.4 km/s). This difference can also be seen in the values for the projected semi-major axis of the system ($a \sin i$). The uncertainty in the radial-velocity of the center of gravity of the system (γ) includes the uncertainty of the radial-velocity in our template star, HD222368 (5.6 $\pm$ 0.3 km/s, Udry et al. 1999). Our calculated masses for the two components in V1143 Cyg are $M_p = 1.355 \pm 0.004 M_\odot$ and $M_s = 1.327 \pm 0.003 M_\odot$. These values lie in between the values calculated by Andersen et al. (1987) $M_p = 1.391 \pm 0.016 M_\odot$ and $M_s = 1.347 \pm 0.013 M_\odot$, and the values given by Giménez & Margrave (1985) $M_p = 1.33 \pm 0.03 M_\odot$ and $M_s = 1.29 \pm 0.03 M_\odot$.

---

[3]Out of eclipse the spectra have a S/N between 40 and 50.

Table 4.2: Derived parameters of V1143 Cyg are given together with their formal errors. The reduced χ^2 of the orbit fit is 0.95 and the reduced χ^2 of the joint fit is 0.96. The average uncertainty in radial-velocity for the primary is 0.16km/s and 0.27 km/s for the secondary, in the joint fit. For comparison, values given by Andersen et al. (1987) and Giménez & Margrave (1985) are also shown. The second and third columns present the parameters obtained in Section 4.3.1. The fourth column shows the parameters derived with the method presented in Section 4.3.2. For the reasons mentioned in Section 4.4 we consider the values found in Section 4.3.2 to be our best parameters and the formal errors given for $v\sin i$ and ζ_{RT} as too small.

Parameter	Center		Shape	Andersen et al. (1987)†
	Orbit	Joint fit		Giménez & Margrave (1985)⋆
T [JD-2400000]	53536.130±0.002	53536.131±0.002	53536.1317±0.0006	
K_p [km/s]	88.1±0.04	88.1±0.1	88.01±0.05	88.2±0.2†
K_s [km/s]	90.1±0.08	90.1±0.2	89.9±0.1	91.1±0.4†
e	0.538±0.001	0.538±0.001	0.5378±0.0003	0.540±0.003†
ω [°]	49.1±0.2	49.1±0.2	49.27±0.05	49.31±0.06⋆
$a\sin i$ [$R_\odot$]	22.67±0.03	22.67±0.03	22.64±0.02	22.78±0.08†
γ [km/s]	−16.8±0.3	−16.8±0.3	−16.8±0.3	−16.5±0.7†
$M_p\sin^3 i$ [$M_\odot$]	1.357±0.005	1.357±0.008	1.350±0.004	1.386±0.016†
$M_s\sin^3 i$ [$M_\odot$]	1.327±0.004	1.327±0.007	1.322±0.003	1.341±0.013†
$v\sin i_p$ [km/s]		16.9±1.0	19.6±0.1	18±2†
$v\sin i_s$ [km/s]		28.0±5.0	28.2±0.1	27±3†
$\zeta_{RT}P$ [km/s]			3.4±0.1	
$\zeta_{RT}S$ [km/s]			3.3±0.1	
β_p [°]		0.5±4.0	0.3±1.5	
β_s [°]		−3.9±4.0	−1.2±1.6	

4.4.2 Stellar parameters

The stellar parameters obtained in Section 4.3.1 are derived by analyzing the shape of the rotation anomaly in the radial velocity. The method relies on a clean subtraction of the foreground star from the obtained spectra before calculating the BF's, which depend on orbital parameters derived from out-of-eclipse measurements, values for the stellar radii, the stellar limb-darkening and the light ratio between the two stars during the subtraction process, which have been taken from the literature.

In Section 4.3.2, the change in the shape of the absorption lines is used instead of the rotation anomaly. Looking at Figs. 4.8 and 4.9, one can see that the simulated BFs are somewhat "rounder" during eclipses than the observed BFs. This can clearly be seen during the central phase of the primary eclipse (Fig. 4.8 panels in the second row) and during the secondary eclipse (Fig. 4.9).

The agreement between the measured BF and the observed BF can be improved if u is included in the fit. The derived values for u would be 0.9 ± 0.1 for the primary and 0.8 ± 0.1 for the secondary. As these values are probably too high (Gray 2005) and the derived values for β would not change significantly ($\beta_p = -0.6 \pm 1.4°$ and $\beta_s = -0.3 \pm 1.2°$), we kept u fixed to 0.6 in the final fits.

Including solar-like differential rotation, the orbital inclination and the stellar radii as free parameters in the fits also leads to a better agreement between data and simulation. However, the derived differential rotation parameters are negative for both stars; the angular rotation speed is faster at the poles than at the equator. Furthermore, the fitted radii are not in agreement with the literature values; the primary radius is increased relative to the literature value and the secondary decreased relative to its literature value. The value for the orbital inclination of V1143 Cyg in the literature is reproduced by our fit, but weakly constrained. A negative differential rotation parameter would give the BFs during the eclipses a more box-like shape. A bigger difference between the stellar radii would further improve the agreement between simulation and data during the central part of the primary eclipse. However, a bigger difference in stellar radii would also mean a bigger difference in stellar masses, which would not agree with the nearly equal semi-amplitudes found in the radial-velocity.

We favor a different explanation for the difference of "roundness" between the measured and simulated BFs. Looking at an absorption line originating from one small area of the stellar disk (i.e. no rotational broadening), the core of an absorption line is formed higher up in the stellar atmosphere than the wings (see Gray 2005), as the same optical depth is reached earlier in the core than in the wings of the absorption line. One can now compare the effect that limb-darkening has on the core and the wings of the absorption lines. In the core of an absorption line, a high optical depth is reached in a high layer of the atmosphere looking down on a stellar atmosphere. This also means that looking from an angle into the stellar atmosphere (i.e. at the limb) will result in a small change in the average height at which the core of the line is formed: Still only the outer cooler parts of the atmosphere are probed. For the wings of the absorption lines the situation is different; the height at which the wings of the observed absorption line are formed changes more from the center to the limb of the stellar disk. Therefore, in going from the center to the limb of a stellar disk the absorption lines become more box-like. The particular shape change

of an absorption line originating under different angles relative to the observer depends
on the details of the stellar atmosphere. This would result in a non-linear limb-darkening
law. Out of eclipse, the light is integrated over the whole stellar surface, but for example,
during the central part of the primary eclipse light is only received from the outer part
of the stellar disk (See Fig. 4.8, icon in the panel of the third column and second row).
Therefore, the shape change of the absorption lines originating from different parts of the
stellar disk might explain the difference between the observed BFs and the simulated BFs
(e.g., Pierce & Slaughter 1982, Balthasar 1988 or Hadrava 2007).

Using the broadening of about 1000 lines, we obtained macro-turbulence parameters
(ζ_{RT}) of 3.4 km/s and 3.3 km/s for the primary and secondary, respectively. For compari-
son, the macro-turbulence parameter found for the Sun, as a disk-integrated star, for weak
and moderately strong lines is $\approx$ 4.0 km/s (Takeda 1995).

The values obtained for the *vsini* of the secondary, using the two different methods
described above, agree with each other and are also consistent with the literature value.
Note that there might be a systematic difference between the obtained radial-velocities of
the secondary during the secondary eclipse and the fit to the radial-velocities (Fig. 4.7).
This might be caused by too high an uncertainty in the orbital parameters used during the
data analysis in Section 4.3.1. The values obtained for the primary *vsini* do agree with
the literature value within their 1-σ error, but do not agree with each other within their
1-σ errors. The method applied in Section 4.3.1 uses the amplitude of the RM effect to
derive the value for the projected rotational velocity. It assumes a linear limb-darkening
coefficient. As mentioned in the last paragraph, this might not be sufficient. Also in
Section 4.3.2 a linear limb-darkening coefficient is used, but *vsini* is derived not only by
the use of the RM effect, but also by the shape of the BF outside of the eclipse. Therefore,
we disregard the value for *vsini* obtained in Section 4.3.1 and take the value of 19.6 km/s
from Section 4.3.2 as the projected rotational velocity for the primary star in V1143 Cyg.
Due to the remaining mismatch between the data and the simulation, which might be due
to the use of too simple a model, we consider the formal errors for ζ_{RT} and *vsini* as too
small.

We would like to point out that the methods used are still in their infancy. Even
with the derived values for the stellar radii, the orbital inclination, limb-darkening and
differential rotation are not free of errors yet; these parameters are not normally accessible,
or only with great difficulty, via spectroscopic data.

4.4.3   Orientation of the rotation axes

The main focus of this work is the robust determination of the orientation of the stellar
rotation axes. The values derived for the projection of the rotation axes onto the plane of
the sky are given in the last two rows of Table 4.2. The βs derived from the two differ-
ent methods agree to within their errors despite the different systematic problems of each
method. Therefore, the projections of the rotation axes of both stars are, to within their
uncertainties, perpendicular to a vector that lies in the plane of the orbit and is perpendic-
ular to the line of sight. What does that mean for the orientation axes of the stars? It is
highly unlikely that the geometry is such that we see the projection of the rotation axes
perpendicular to the orbital plane, but that the stellar rotation axes have a high inclination
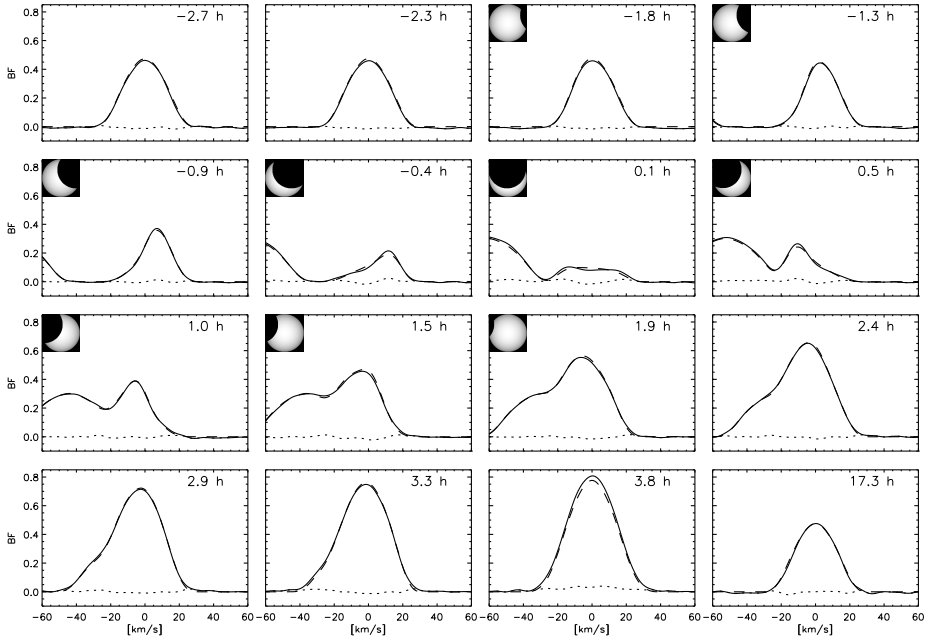
Figure 4.8: BFs during the primary eclipse centered in the frame of the primary. Each panel represents one measurement. The solid line represents the measured BF, the dashed line shows the best fit BF, while the dotted line represents the difference between the fit and the measurement. The numbers in the upper right corner of each observation indicate the time difference between the midpoint of the observation and the midpoint of the eclipse in hours. In the upper left corner one can see the uncovered part of the primary half-sphere for the midpoint of that measurement if the star was eclipsed during this measurement. One can see that the BF of the secondary moves closer to the primary BF in velocity space over the course of the eclipse. Please note that the scale of the ordinate is arbitrary. The panel in the lower right corner shows the BF of the primary for an observation out of eclipse.

towards the observer. We therefore conclude that the stellar rotation axes are normal to the orbital plane, and aligned with each other and the rotation axis of the system.

This leaves the theoretical prediction of the apsidal motion unaltered for V1143 Cyg. Hence, the difference between expected ($0.00089 \pm 0.00015°$/cycle) and measured apsidal motion ($0.000705 \pm 0.000041°$/cycle), which just lies outside the 1-σ error bars, is also unchanged. The effect of a misalignment between the stellar rotation axes and the orbital spin axis on the apsidal motion has been studied by Kopal (1978), Shakura (1985), Company et al. (1988), and Petrova & Orlov (2003). The contribution of the stellar rotation to the advance of the longitude of the periastron is reduced if the stellar rotation axis is tilted
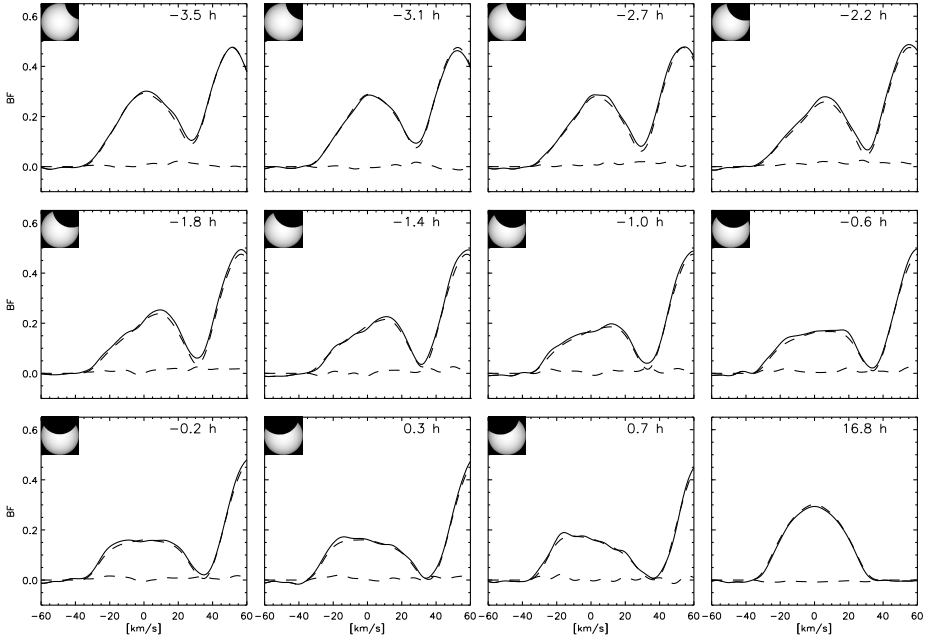
Figure 4.9: The same as Fig. 4.8 but for the secondary eclipse. One can see that the BF of the primary moves further away from the secondary BF in velocity space over the course of the eclipse. The panel in the lower right corner shows the BF of the secondary for an observation out of eclipse.

against the orbit spin axis until finally, when the axis of stellar rotation lays in the orbital plane, its contribution is half as large and with the opposite sign as when the stellar and orbital axes would be parallel. In this situation, it contributes to a retrograde rotation of the periastron. The contribution of the stellar rotation to the apsidal motion depends not only on the orientation of the axis, but also on the square of the angular stellar rotation rate. As one measures only $v \sin i$, a greater inclination towards the observer would mean a higher angular stellar rotation rate, and therefore a greater contribution of the rotation term to the overall apsidal motion. We derive that if the rotation axes of both stars would lie in the orbital plane, but have no inclination towards the observer, then the complete apsidal motion would be $0.00073°$/cycle. If the rotation axes would have an inclination towards the observer of $i \approx 70°$ in either of the two stars, or of $i \approx 60°$ in both stars, only then would the expected and measured apsidal motion be in agreement. The secondary, due to its higher $v \sin i$, has a larger influence on the rotational term of the apsidal motion than the primary component. As already pointed out, it is very unlikely that the stellar and orbital spin axes span a large angle, while their projections on the sky are, in their uncertainties, parallel. Our findings do not support the hypothesis advocated by Petrova & Orlov

(2003), that a misalignment of the stellar rotation axes with the orbital spin could bring the theoretical and measured apsidal motion for a number of binary systems, including V1143 Cyg, into better agreement.

Our work has excluded the option of a misalignment between the stellar rotation axes as a possible explanation for the difference between the expected and measured apsidal motion in V1143 Cyg. It is therefore interesting to look at other possibilities that might explain this difference. As the apsidal motion constant (k_2) is an important source of uncertainty in the calculation of the expected apsidal motion, a new calculation of the apsidal motion constant for V1143 Cyg using modern codes for stellar evolution might be of value.

In our analysis of the orbital data we found no indication of a third body in the V1143 Cyg system, whose influence might also alter the apsidal motion. However, because of the limited coverage in time (one year) and the limited accuracy in radial-velocity, combined with the possibility that the orbit of a third body could have a lower inclination, a third body cannot be excluded.

The alignment of the stellar rotation axes could also set a lower limit to the age of the system, if the axes were not aligned at the birth of the system. However, this is not a straightforward argument, since, during the pre-main-sequence phase, synchronizing forces must have been larger, due to the larger sizes of the stars. Proper modeling of the evolution of V1143 Cyg might reveal whether it had enough time to align its axes. If the time-span to align the axes is longer than the lifetime of the system, it would mean that V1143 Cyg, with its high eccentricity of 0.54, was born in this way, with all spin and orbital axes aligned.

4.5 Conclusions

We measured the Rossiter–McLaughlin effect for both components in the binary system V1143 Cyg. We developed two different methods to derive the angle β between the stellar spin axis projected onto the plane of the sky and the orbital spin axis projected onto the plane of the sky.

Using the first method, i.e. by determination of the center of the broadening function, we showed how it is possible to subtract the absorption lines of the foreground star during an eclipse from the spectrum. This made it possible to use the shift of the center of gravity of the absorption lines as a proxy for the rotation effect, even in systems with blending occuring during eclipses, and derive values for β and *vsini*. However, for systems with low eccentricity, blending of the spectral lines during eclipses is stronger than in V1143 Cyg. Therefore, every systematic error in the tomography or in the subtraction of the foreground spectrum due to the parameters used in the subtraction, will have a substantial effect on the value of β derived.

The second method presented in this chapter, the modeling of the shape of the broadening functions, avoids the problems of the first method by taking the influence of the eclipsing star into account explicitly. This makes the method more suitable for eclipsing binary systems with low eccentricity (higher blending of the spectral lines). The use of the complete BFs, instead of the center of gravity or the Gaussian fit to the line, has the

additional advantage that it makes the fitting of the parameters β and *vsini* more precise. However, the derived values for these parameters are not necessarily free of systematic errors. Further work is needed here to make it possible to derive information about velocity fields on the stellar surface represented by macro-turbulence, or differential rotation. If differential rotation is present it might be possible to derive some information about the inclination of the rotation axes towards the observer.

With both methods we determined orbital and stellar parameters which agree within their uncertainties with values derived in earlier studies, with the exception of the semi-amplitude of the secondary. The values derived for the angle β agree with each other. We found that the stellar rotation axes in V1143 Cyg are normal to the orbital plane for both components, which leaves the theoretical predictions for the apsidal motion unchanged. This makes V1143Cyg the first binary system with main-sequence stars for which the orientations of the rotation axes of both components are determined.

Even with progress made in the field of apsidal motion in the last years (e.g. Claret & Willems 2002), it is interesting to apply the methods discussed here to other binary systems where there is a stronger disagreement between the observed and expected apsidal motion (e.g. DI Herculis, Claret 1998), in order to investigate whether a misalignment of the stellar rotation axes can be excluded as a cause for the disagreement, or a misalignment contributes to the difference. Furthermore, information about the orientation of the stellar rotation axes in binary systems could be used to explore the dependence of the synchronization time scales on the semi-major axis, eccentricity of the binary system and the stellar type of its components. This might lead to new insight about the formation and evolution of binary systems and stellar interiors.

Acknowledgments

4.6 Data

Table 4.3: Radial velocity measurements of V1143 Cyg out of eclipse and during the primary and secondary eclipse. The photon midpoints of the observations are given in the first column, while the radial velocities of the primary and secondary are given in the second and third row.

HJD	Vel. P	Vel. S
[JD-2400000]	[km/s]	[km/s]
53612.665	35.40±0.13	−81.71±0.22
53612.683	30.58±0.14	−76.43±0.23
53651.654	−71.40±0.14	27.82±0.22
53613.663	−76.90±0.14	33.40±0.23
53613.771	−78.44±0.14	34.56±0.22
53613.880	−79.27±0.14	35.48±0.23
53934.843	−79.49±0.14	35.83±0.23
53583.676	−78.86±0.14	35.39±0.23
53936.818	−57.40±0.13	13.47±0.22
53585.669	−51.69±0.15	6.91±0.25
53649.639	43.23±0.14	−89.43±0.23
53611.709	62.33±0.14	−109.40±0.23
53611.728	63.65±0.14	−111.21±0.24
53611.814	70.69±0.13	−117.65±0.22
53611.835	72.30±0.14	−119.47±0.23
53611.884	76.29±0.14	−123.12±0.23
53611.903	77.69±0.13	−125.03±0.22
53932.846	80.45±0.13	−127.61±0.22
53581.675	96.71±0.14	−144.12±0.24
53650.612	88.17±0.14	−135.32±0.23
53650.737	67.50±0.14	−113.86±0.22
53612.865	−12.10±0.18	−33.23±0.27
53612.884	−15.74±0.19	−29.58±0.28
53612.901	−19.29±0.18	−26.26±0.28
53612.919	−22.44±0.18	−22.26±0.27
53579.678	−11.09±0.18	−33.60±0.28
53612.701	27.01±0.20	
53612.719	24.88±0.20	
53612.737	22.93±0.20	
53612.757	18.28±0.20	
53612.775	6.63±0.20	
53612.793	−2.84±0.20	
53612.811	−5.44±0.20	

continued on next page

Table 4.3: Radial velocity measurements of V1143 Cyg

HJD	Vel. P	Vel. S
[JD-2400000]	[km/s]	[km/s]
53612.829	-6.75 ± 0.20	
53612.847	-8.71 ± 0.20	
53587.717		-46.88 ± 0.32
53587.732		-46.88 ± 0.32
53587.748		-46.85 ± 0.32
53587.767		-47.20 ± 0.32
53587.782		-47.74 ± 0.32
53587.798		-48.19 ± 0.32
53587.816		-50.23 ± 0.32
53587.832		-52.14 ± 0.32
53587.848		-53.93 ± 0.32
53587.866		-56.31 ± 0.32
53587.882		-57.96 ± 0.32

Bibliography

Andersen, J., Nordstrom, B., Garcia, J. M., & Giménez, A. 1987, A&A, 174, 107 58, 59, 62, 67, 68

Bagnuolo, Jr., W. G. & Gies, D. R. 1991, ApJ, 376, 266 64

Balthasar, H. 1988, A&AS, 72, 473 70

Claret, A. 1998, A&A, 330, 533 74

Claret, A. & Willems, B. 2002, A&A, 388, 518 74

Company, R., Portilla, M., & Gimenez, A. 1988, ApJ, 335, 962 71

ESA. 1997, ESA SP-1200 58

Giménez, A. 2006, ApJ, 650, 408 58

Giménez, A. & Margrave, T. E. 1985, AJ, 90, 358 58, 59, 62, 67, 68

Gray, D. F. 2005, The Observation and Analysis of Stellar Photospheres (The Observation and Analysis of Stellar Photospheres, 3rd Edition, by D.F. Gray. ISBN 0521851866. Cambridge, UK: Cambridge University Press, 2005.) 66, 69

Hadrava, P. 2007, in Astronomical Society of the Pacific Conference Series, Vol. 370, Solar and Stellar Physics Through Eclipses, ed. O. Demircan, S. O. Selam, & B. Albayrak, 164 70

Hosokawa, Y. 1953, PASJ, 5, 88 58, 65

Hube, D. P. & Couch, J. S. 1982, Ap&SS, 81, 357 58

Kopal, Z. 1959, Close binary systems (The International Astrophysics Series, London: Chapman & Hall, 1959) 58, 65

Kopal, Z., ed. 1978, Astrophysics and Space Science Library, Vol. 68, Dynamics of Close Binary Systems 71

McLaughlin, D. B. 1924, ApJ, 60, 22 58

Ohta, Y., Taruya, A., & Suto, Y. 2005, ApJ, 622, 1118 58

Petrova, A. V. & Orlov, V. V. 2003, Astrophysics, 46, 329 71, 72

Pierce, A. K. & Slaughter, C. 1982, ApJS, 48, 73 70

Press, W. H., Teukolsky, S. A., Vetterling, W. T., & Flannery, B. P. 1992, Numerical recipes in FORTRAN. The art of scientific computing (Cambridge: University Press, |c1992, 2nd ed.) 61, 67

Queloz, D., Eggenberger, A., Mayor, M., et al. 2000, A&A, 359, L13 58

Rossiter, R. A. 1924, ApJ, 60, 15 58

Rucinski, S. 1999, in ASP Conf. Ser. 185: IAU Colloq. 170: Precise Stellar Radial Velocities, ed. J. B. Hearnshaw & C. D. Scarfe, 82 61

Shakura, N. I. 1985, Soviet Astronomy Letters, 11, 224 71

Snellen, I. A. G. 2004, MNRAS, 353, L1 58

Takeda, Y. 1995, PASJ, 47, 337 70

Udry, S., Mayor, M., Maurice, E., et al. 1999, in ASP Conf. Ser. 185: IAU Colloq. 170: Precise Stellar Radial Velocities, ed. J. B. Hearnshaw & C. D. Scarfe, 383 61, 67

Winn, J. N., Johnson, J. A., Marcy, G. W., et al. 2006, ApJ, 653, L69 58

Worek, T. F. 1996, PASP, 108, 962 58